3-2020

Determining Bulk Aerosol Absorption from Off Axis Backscattering using Rayleigh Beacon Laser Pulses

Julie C. Grossnickle

DETERMINING BULK AEROSOL ABSORPTION FROM OFF-AXIS BACKSCATTERING USING RAYLEIGH BEACON LASER PULSES

THESIS

Julie C. Grossnickle, Captain, USAF

AFIT-ENP-MS-20-M-097

DEPARTMENT OF THE AIR FORCE
AIR UNIVERSITY

AIR FORCE INSTITUTE OF TECHNOLOGY

Wright-Patterson Air Force Base, Ohio

AFIT-ENP-MS-20-M-097

DETERMINING BULK AEROSOL ABSORPTION FROM OFF-AXIS BACKSCATTERING USING RAYLEIGH BEACON LASER PULSES

THESIS

Presented to the Faculty

Department of Engineering Physics

Graduate School of Engineering and Management

Air Force Institute of Technology

Air University

Air Education and Training Command

In Partial Fulfillment of the Requirements for the

Degree of Master of Science in Atmospheric Science

Julie C. Grossnickle, MS

Captain, USAF

March 2020

AFIT-ENP-MS-20-M-097

DETERMINING BULK AEROSOL ABSORPTION FROM OFF-AXIS BACKSCATTERING USING RAYLEIGH BEACON LASER PULSES

Julie C. Grossnickle, MS

Captain, USAF

Committee Membership:

Dr. S. T. Fiorino
Chair

Dr. K. J. Keefer
Member

Lt Col R. C. Tournay, PhD
Member

Lt Col H. R. Tseng, PhD
Member

Abstract

Aerosol absorption and scattering can play a key role in degrading high energy laser performance in the form of thermal blooming and beam attenuation. Aerosol absorption properties are not completely understood, and thus affect how we are able to quantify expected high energy laser weapon performance. The Air Force Institute of Technology Center for Directed Energy (AFIT CDE) developed both Laser Environmental Effects Definition and Reference (LEEDR) and the High Energy Laser End-to-End Operational Simulation (HELEEOS) code to characterize atmospheric radiative transfer effects and evaluate expected directed energy weapon system performance. These packages enable modeling of total irradiance at given off-axis locations through the use of an off-axis scattering algorithm, which uses scattering phase functions to predict the amount of radiation scattered from the beam toward a particular observation location. Laser energy scattered from a Rayleigh beacon illuminator at 527 nm, located at the John Bryan Observatory (JBO) in Yellow Springs, Ohio, is measured using a high resolution Mini-Shortwave Infrared (SWIR) snapshot camera. Aerosol characterization information was gathered using a Condensation Particle Counter (CPC), a Scanning Mobility Particle Sizer (SMPS) spectrometer, and a Continuous Light Absorption Photometer (CLAP). The differences in the measured versus predicted phase functions can help draw conclusions relative to bulk aerosol absorption properties, and lead to better quantification of degradation of laser performance due to aerosols.

Acknowledgments

I would like to express my sincere gratitude to my advisor Dr. Steven Fiorino for the continuous support throughout my research, as well as patience, motivation, enthusiasm, and immense knowledge. Without his guidance this thesis would not be complete. I'd also like to thank Dr. Kevin Keefer, who assisted me throughout the entire data collection process and equipment maintenance, and gave me considerable help in the concepts necessary to analyze my data. I owe thanks to Aaron Archibald, Ben Wilson, Joel Meoak, and Brannon Elmore, for all their system support throughout this project. Additionally, I would like to thank the team at JBO Steve Zuraski and the entire Applied Optimization crew for their flexibility and support at the laser site. My sincere thanks also goes to my meteorology faculty Lt Col Tournay, Lt Col Tseng, and Maj Nava, for their encouragement, insight, and support.

Last but not least, I would like to thank my classmates, friends, and family for their continued support, frequent sources of amusement, perspective, and most of all, patience.

Julie C. Grossnickle

Table of Contents

Page

List of Figures

List of Acronyms

AFIT - Air Force Institute of Technology

AO – Adaptive optics

CDE – Center for Directed Energy

CIR – complex index of refraction

CLAP – continuous light absorption photometer

CPC – condensation particle counter

EM – electromagnetic

ExPERT - Extreme and Percentile Environmental Reverence Tables

FOV – field of view

FPA – focal plane array

GADS - Global Aerosol Data Set

HEL – high energy laser

HELEEOS – High Energy Laser End-to-End Operational Simulation

InGaAs – Indium Gallium Arsenide

INSO – water-insoluble

IR – Infrared

LEEDR – Laser Environmental Effects Definition and Reference

MAGIC - Moderated Aerosol Growth with Internal water Cycling

MC - mineral

NOAA – National Oceanic and Atmospheric Association

NWP – numerical weather prediction

OPAC – Optical Properties of Aerosols and Clouds

RTE – radiative transfer equation

SMPS – scanning mobility particle sizer

SS – sea-salt

SUSO – sulfate solution

SWIR – shortwave infrared

WASO – water-soluble

DETERMINING BULK AEROSOL ABSORPTION FROM OFF-AXIS BACKSCATTERING USING RAYLEIGH BEACON LASER PULSES

I. Introduction

Aerosols have a wide range of impacts in the natural atmosphere--direct, indirect, and semi-direct. The first--direct effect--is the heating or cooling of the atmosphere through absorption and scattering of both solar and terrestrial radiation. The second--indirect effect--are the changes to the microphysical and radiative properties of clouds from aerosols acting as cloud condensation nuclei. The third--semi-direct effect--which is the 'cloud burning effect' by heating the atmosphere. Here, absorbed solar radiation heats the cloud, reducing cloud cover and liquid water content (Hansen et al. 1997). The full extent of these aerosol effects are still not wholly understood, and the quantification and measurement of aerosol absorption properties remain a challenge.

A *fourth* effect of aerosols is when the particles interact with the purposeful propagation of concentrated electromagnetic (EM) energy, such as laser beams. Aerosols can degrade laser performance through thermal blooming--a spreading of the beam due to interaction between absorbed laser radiation and the propagation medium, much like the semi-direct effect--and beam attenuation--removed or re-directed laser light as a result of absorption and scattering of the laser beam.

All four effects stemming from the presence of aerosols can affect military capabilities involving targeting, communication, directed energy weapons, and sensor performance. In particular, as high energy lasers become more prevalent in defense operations, the ability to quantify degradation of laser performance due to aerosols becomes increasingly more important. Furthermore, understanding aerosol optical

properties from laser energy propagation can have implications for the atmospheric science communities at large.

The purpose of this research is two-fold--first, to test the hypothesis that measured off-axis backscatter from high energy lasers can be used to determine bulk aerosol absorption, and second, to develop a technique that can be applied in both high energy laser applications and within atmospheric science communities. The technique involves using a beacon laser, associated with HEL (weapons system or other), and a camera sensor to measure aerosol backscatter, compare to LEEDR and HELEEOS model output, and back out aerosol absorption properties. Furthermore, the overall objective is to be able to infer bulk aerosol absorption using a simple particle counter and a radiative transfer model like LEEDR.

1.1 Background

Atmospheric scattering consists of both forward and backward directional components. Molecules and aerosol particles cause light to be scattered out of the beam in all directions, where the scattering toward the laser beam, or origin of the light source, is known as backscatter, and scattering in the same direction, or away from the origin of the light source, is known as forward scattering. The direction of the scattering is dependent on the particle size and wavelength of the light. Particles that are much smaller than the wavelength of a laser beam scatter equally in a forward and backward direction, while larger particles scatter more strongly in the forward direction.

It is possible to characterize a laser through remote (off axis) observation of the laser beam scatter. With the atmospheric environment and particle counts sufficiently characterized and the following attributes of the laser beam known: location in reference

to the observation point, azimuth, elevation, power, off-axis point, scattered irradiance can be calculated.

This research employs numerical modeling packages, an off-axis scattering algorithm, as well as experimental equipment.

The modeling packages--LEEDR and HELEEOS--were developed by AFIT CDE to characterize radiative transfer effects and simulate laser propagation through the atmosphere (Bartell et al, 2005). These packages together enable calculation of total irradiance at given off-axis locations through the use of scattering phase functions. HELEEOS was developed for the purpose of evaluating expected directed energy weapon system performance. It predicts the properties of a high energy laser beam at every point along its path, account for atmospheric interaction, while fully incorporating a probabilistic climatological database (Fiorino et al, 2006). Recognizing that the capability to create realistic data profiles of the atmospheric effects on EM propagation extended beyond directed energy weapon performance analysis, AFIT CDE produced LEEDR. The LEEDR model is a worldwide surface-to-100 km, ultraviolet-to-radio frequency, atmospheric characterization package. It defines the well-mixed atmospheric boundary layer with a probabilistic surface climatology, and then computes the radiative transfer and propagation effects from the vertical profile of meteorological variables. It also has the capability for users to directly input surface observations, surface aerosol number concentrations, or numerical weather prediction (NWP) data in lieu of the climatological profile (Fiorino et al, 2014).

Developed by Scott Belton in 2006, the initial off-axis scattering algorithm was added to HELEEOS in order to provide the model with the computational tools to output

scattered irradiance, given known properties of a laser, at any off-axis location (Belton, 2006). The algorithm takes a given laser power and wavelength input, the relative bulk aerosol particle size, and bulk characteristic phase function profile, and calculates the scattered irradiance at any off-axis observer location. Aerosol particle count and size distribution can be taken from a climatology database coupled with HELEEOS, or input by the user from actual measured aerosol number concentrations. The scattering angles and their location on the beam are determined using standard geometry calculations as long as the length of the laser beam path and distance to the off-axis observation point are known.

The algorithm determines the amount of scattered irradiance for separate sections of the beam. It splits the beam into 1,000 separate segments, *i*, accounting for phase angles, cross sections of scattering particles, and the number density of each particle. Scattering angles, shown in Figure 1below, are computed using standard geometrical relationships. A full description on how the algorithm computes scattering angles can be found in Belton, 2006.

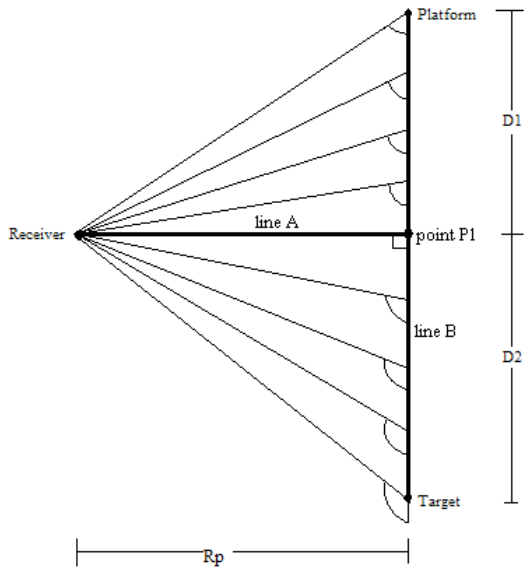

Figure 1. HELEEOS off-axis algorithm schematic of geometric set-up for off-axis irradiance calculations and beam segment breakdown (Fiorino et al, 2010).

With the scattered irradiance and phase angles of each segment calculated, the amount that reaches a given off-axis location are determined using transmittance calculations by simulating a laser beam from each segment to the off-axis point. Each simulated laser beam is equal to that of the calculated scattered irradiance of its respective segment. Transmittance is determined by accounting for extinction along the simulated beam path associated with the atmosphere defined by the user. The end equation used within the algorithm is,

$$I_{SCA} = \sum_{i=1}^{1000} \frac{P(\theta)\beta_{SCAi} I_{Oi} t_i}{4\pi R_i^2} dv_i \quad (1)$$

where I_{SCA} is the scattered intensity that reaches the off-axis observing point, $P(\Theta)$ is the scattering phase function, β_{SCA} is the volume scattering coefficient. I_{Oi} is the initial beam intensity, t_i is transmittance, R_i is the distance between the receiver and the beam, and dv_i is the scattering volume (Belton, 2006; Fiorino et al, 2010).

John Haiducek (2010) experimentally tested and validated the off-axis algorithm capability using an infrared camera and two infrared lasers, with a power range of 1 to 5 watts and a wavelength of approximately 1550 nm, at Wright-Patterson Air Force Base in July 2009. Infrared images of the laser beam were taken from an off-axis location and irradiance values were computed from the image pixels. Those values were then compared to that of the HELEEOS off-axis scattering algorithm output. The analysis of the tests revealed that HELEEOS outputs correlated weakly to the measured irradiances, and produced outputs nearly two orders of magnitude different than the measured irradiances. Although the data was not in close enough agreement to serve as a validation of the algorithm by itself, there was some correlation in terms of laser power output and viewing angle. As such, this test showed that this method can be successfully used to calculate the intensity of off-axis scattering and infer scattering phase function profiles (Haiducek, 2010; Fiorino et al, 2010).

The techniques Haiducek developed to validate the off-axis scattering algorithm provided the basis for the methods used to test the hypothesis that backscatter from a high energy laser beam can be used to determine bulk aerosol absorption. Experimental equipment involved in this research included a commercially available, standard charge-coupled device (CCD) visible camera (i.e. Canon Sure-Shot), and an ultra-fast laser.

The experiments conducted in this research are similar to those conducted by Haiducek (2009), except instead of a visible CCD camera, he used an infrared camera equipped with an Indium Gallium Arsenide (InGaAs) focal plane array (FPA) to capture laser energy. Additionally, his receiver telescope was placed at an off-axis location to measure forward scattered irradiance.

The experiments are different from those conducted by Haiducek (2009) in that this research measured backscatter rather than forward scattering, the experiment geometry was different, and an ultrafast Rayleigh beacon pulse laser was used as the energy source.

The main difference in the experiment geometry was the elevation angle of the laser beam. The laser beam was pointed into the sky at a 45^{o} elevation angle, as opposed to horizontally at a target in the distance, as Haiducek did. The degree of elevation angle is not important, only that the laser beam is pointed to the sky. This setup allows for a longer laser beam length for analysis, and changes in scattered energy with altitude for examination.

1.2 Motivation

Aerosol absorption properties are not completely understood yet can significantly affects high energy laser weapon performance. By employing methods developed in Haiducek's research while exploiting pulsed-beacon lasers and leveraging the knowledge of laser attenuation, and its degradation along the laser beam path, the hypothesis that measured off-axis backscatter from high or low energy lasers can be used to determine bulk aerosol absorption can be tested. Uses for this research include lasers, remote sensing, and defense applications. Additionally, this knowledge can be applied in both the atmospheric science and climate assessment research communities.

1.3 Overview

This document summarizes the current understanding of aerosol absorption and scattering properties and their effect on directed energy applications in Chapter 2. Chapter 3 describes the methods in which data is acquired concerning off-axis

backscattered laser energy phase functions and aerosol characterization information. It also explains the process of both incorporating data into LEEDR and using the off-axis backscattering algorithm used in HELEEOS to obtain predicted phase functions. Chapter 4 covers data analysis and explores the findings from analyzing visible laser images and modeled phase functions. Lastly, Chapter 5 summarizes results and discusses how this research can be incorporated into future work.

II. Literature Review

2.1 Laser Propagation

A laser is a nearly monochromatic, highly coherent radiation that propagates in a well-defined direction, and is produced through simulated emission (Perram et al, 2010). The laser propagates through the air as a narrow beam of light at the speed of light and places a small spot of light on a target. However, laser beams often suffer degradation as it propagates through the atmosphere. Many variables can affect laser performance but atmospheric conditions play a large role.

The HEL, originally developed as a means to reduce the threat of nuclear war, is a weapon system for mainly defensive military applications. The benefit of a laser weapons system lies in the fact that it expends stored energy rather than munitions. Its lethality mechanism is thermal damage and includes burning, melting, structural failure, and or thermal penetration (Perram et al, 2010).

In order for a HEL to be effective it must have laser lethality--capability to render a target nonfunctional. There are several factors to consider in determining laser lethality. Those factors include power and wavelength of the laser, diameter of the primary mirror (spot size), range to the target, time on target (dwell time), and delivered irradiance. In

other words, the delivered fluence--the accumulated laser irradiance at a target over a period of time--needs to exceeds the target's threshold for damage. A major factor of delivered fluence is beam quality--measure of the ability to tightly focus a laser beam to a small spot on the target (Perram et al, 2010). This is true even for non-weapon laser systems like communications and target illumination.

A variety of factors reduce delivered fluence, but the state of the atmosphere has a large influence on laser system performance (Perram et al, 2010). Variability in performance is dominated by the variability in atmospheric conditions, thus there is a need for the ability to properly model atmospheric impacts to HEL propagation in order to assess engagement limitations.

Atmospheric conditions mainly cause degradation to spot size and power through optical turbulence, thermal blooming, and atmospheric extinction. Optical turbulence and thermal blooming--distortions in the wave front due to variance in the index of refraction from temperature variations--cause a laser beams to deviate as it propagates through atmosphere. These deviations create intensity fluctuations and blur the beam to a larger spot size, thus spreading the energy and reducing delivered irradiance. Extinction, the sum of absorption and scattering, is of cardinal importance in calculating the overall loss of laser energy along a path. Atmospheric absorption and scattering attenuate laser power at varying degrees dependent on wavelength, and the irradiance transmission can decay significantly with range. Additionally, absorption can induce thermal blooming by heating atmospheric gases within the beam, producing a gradient in the index of refraction that shifts the beam away from the intended direction of propagation (Perram

et al, 2010). Thus, characterization atmospheric absorption and scatter is important to laser system performance assessments.

All high energy laser systems have some sort of beam control system in order to ensure high beam quality. These control systems usually include adaptive optics (AO), which involves a beacon laser to probe the atmosphere (Perram et al, 2010). AO can correct for the degradation effects of optical turbulence and thermal blooming on beam propagation; however, there is no direct way to correct for loss of energy from absorption and scattering. This reduction from absorption and scattering requires longer dwell time on target because of the linear relationship between delivered fluence and dwell time. The lower the amount of fluence the longer the dwell time required to surpass lethal fluence.

Atmospheric extinction is a complex beast to quantify due to spatial and temporal variations in suspended particles, especially with aerosols. Further research with HEL has the potential to significantly enhance mission planning tools. At the very least using HEL or beacon pulse lasers to determine absorption properties can provide a method to quickly quantify atmospheric degradation and thus how long a laser spot must remain on a target.

2.2. Atmospheric Extinction

Gases and particulates suspended in the atmosphere degrade transparency by absorbing and scattering light. This is known as atmospheric attenuation or extinction – the reduction in the intensity of a directly transmitted beam of radiation as it passes through the atmosphere. Intensity with respect to EM radiation is the rate of emitted energy from a unit surface area through a unit solid angle. The total amount of extinction is proportional to the intensity of the incident radiation, and is the sum of both absorption

and scattering from gas molecules and other particles--aerosols and liquid and ice particles--suspended in the atmosphere.

Gas molecules (primarily nitrogen, oxygen, argon, carbon dioxide, and water vapor) both scatter and absorb radiation. Some, like nitrogen and oxygen, are present in the atmosphere in nearly unvarying concentrations, while others, like water vapor and carbon dioxide, are highly variable from one time and/or location to another. In the absence of clouds, absorption by molecules controls the overall opacity of the atmosphere, mostly by the less abundant or variable molecules. However, gas molecules can significantly scatter radiation, mostly at shorter wavelengths (Petty, 2006).

There are also countless small particles of dust, salt, and other materials suspended in the air, known as aerosols. Both absorb and scatter radiation and are also highly variable in concentration from one time and location to another. Whether aerosols scatters or absorbs radiation along a path, or both, depends on the size and composition of the particle. Unlike gas molecules, the contribution of aerosols to the extinction of radiation in the atmosphere cannot be generalized because their composition and concentration are so highly variable (Petty, 2006).

Additionally, aerosols can have a cooling effect at lower altitudes by extinguishing incoming radiation, but there is uncertainty in exactly how much of a cooling effect they have. Radiation absorption from aerosols transforms EM energy into thermal energy, which can alter temperatures, relative humidity, and cloud formation, and thus have implications on atmospheric circulations and stability (Moosmuller et al., 2009). Currently, the ability to capture the magnitude of the impact aerosols have on atmospheric circulations is limited.

Aerosol absorption both attenuates and thermally blooms laser energy beams, which significantly degrades directed energy applications such as HEL targeting (Burley et al., 2017). The ability to quantify the magnitude of these impacts is limited by the measurement and calculation techniques that are based on our understanding of EM energy absorption and scattering theories.

Fortunately, absorption properties can be inferred, or at least approximated, from scattering and extinction properties and therefore, this research focuses on measuring scattering properties from a HEL. This chapter summarizes the fundamental concepts and theories of scattering and the phase function. A summary of laser propagation and scattering applications is also included as a prelude for discussion on viability of using the presented method to determine bulk aerosol absorptions and characterize laser performance degradation.

2.3 Scattering

When radiation is scattered, its energy is redirected, and therefore, the loss of radiation along one directional path results in a gain in another direction(s). This is how laser beams are observed: scattered light is redirected to your eyes. If there were no particles in the air to scatter visible radiation, the beam would not be visible off-axis.

In order to determine the change in intensity along a finite path, absorption and scattering, both as a source of extinction as well as a source of radiation into the path, must be accounted for. Typically, scattering as a source of radiation into the path of interest (dI_{scat}) is ignored in radiative transfer calculations. This is perfectly acceptable to do when gains in intensity from scattering into the directional path of interest is

negligible compared to losses due to extinction and gains from thermal emissions (Petty, 2006).

Neither absorption nor scattering properties are directly measured, rather they are derived and calculated using extinction measurements. Absorption properties are determined by subtracting scattering from extinction, and scattering properties are calculated through scattering theory equations based on particle size and shape, composition, and number concentration.

The general form of the radiative transfer equation (RTE) accounting for extinction, emission and scattering into the beam, respectively, can be expressed as

$$dI = dI_{ext} + dI_{emit} + dI_{scat}, \tag{2}$$

where, dI_{ext}, is the extinction component and is defined as

$$dI_{ext} = -\beta_e I ds. \tag{3}$$

Since this research uses a visible light source and assumes single scatter as the predominate source of scattered light at the observation location, the focus is only on the extinction component of the RTE. The scattering portion of the extinction component, depends on the local extinction coefficient by volume, $\beta_{e,}$ the single scatter albedo, $\acute{\omega}$, and the scattering phase function, $p(\Theta)$ - the angular distribution of radiation intensity scattered by a particle at a given wavelength. These, in turn, depend on both wavelength and the suspended particles' size, composition, shape, and number concentration. For scattering specifically, the size of the particle is the most important defining characteristic (Petty, 2006).

2.3.1 Extinction, Scattering, and Absorption Coefficients

As already mentioned, the extinction along a path is the sum of the scattered and absorbed radiation. When calculating the extinction portion of the RTE, the absorption and scattering coefficients, β_a and β_s, are used to represent absorption and scattering by volume. In order to solve scattering and absorption specifics from extinction, it is helpful to determine the relative importance of scattering versus absorption within a medium. This is determined through the use of the single scatter albedo, $\acute{\omega}$, which is the ratio of scattering to extinction an can be expressed as

$$\acute{\omega} = \frac{\beta_s}{\beta_e} = \frac{\beta_s}{\beta_s + \beta_a}. \quad (4)$$

Scattering, absorption, and extinction coefficients can not only be defined in terms of volume, but also in mass-normalized and particle-normalized terms. In fact, these terms are often used rather than the terms used in reference to a fixed geometric distance (Petty, 2006). For example, the Weather Research and Forecast with Chemistry model quantifies atmospheric aerosols by mass densities, and LEEDR, specifically for Mie calculations, directly uses number concentrations to determine extinction, scattering, and absorption coefficients (Barnard et al. 2010, and Fiorino et al. 2019).

The mass-normalized extinction term, known as the mass extinction coefficient k_e, is expressed in terms of density and mass per unit area. It relates the volume extinction coefficient to the density of air particles.

$$\beta_e = \rho k_e \quad (5)$$

When considering that the atmosphere includes a mixture of a variety of particles, the total mass extinction coefficient is then sum of the individual mass extinction for each

type of particle (Petty, 2006). The use of the mass extinction term is commonly used when dealing with highly variable atmospheric constituents like water vapor. Mass extinction is constant for most substances in the atmosphere as long as all other variables, like pressure and temperature, are held constant. Aerosol mass densities is the legacy variable used in aerosol quantification and reporting, and in fact there is a wide network of accessible aerosol databases and networks that document mass density information for several of the different aerosol types (Hess et al. 1998, Andrews et al. 2019, and Koepke et al. 1997).

The particle-normalized extinction term, known as the extinction cross section σ_e, is expressed in terms of particle number concentrations. It relates the volume extinction coefficient to the number concentration, N.

$$\beta_e = \sigma_e N \tag{6}$$

The extinction cross section, refers to a single particle, so once again when dealing with a mixture of a variety of particles, there are multiple cross section values and number concentrations to consider (Petty, 2006). The use of the extinction cross section is common when calculating radiative transfer through clouds. Using number concentrations, which can be easily measured rather than approximated, allows for increased accuracy of microphysical schemes, which could have significant implication on reliable numerical modeling of climate change (Fiorino et al. 2019, Peralta and Enrique 2013).

Recalling that extinction is the sum of absorption and scattering, separate mass-normalized and particle-normalized quantities for absorption and scattering coefficients can also be defined.

2.3.2 Rayleigh Scattering, Mie Scattering, and the Phase Function

Scattering and absorption properties of an aerosol particle is dependent on the relationship between the size and composition of the particle, and the wavelength of the radiation of interest. These same characteristics are also of crucial factors in determining a suitable method for calculating those properties (Petty, 2006). For scattering, the size of the particle is the most important characteristic, while for absorption, particle composition, or specifically the particle's complex index of refraction (CIR), is the most important characteristic. In general, particles that are much smaller than the wavelength weakly scatter radiation, and particles that are much larger than wavelength scatter more strongly. Furthermore, particle size and shape also have an impact on whether radiation is more strongly scattered in the forward or both forward and backward directions, which is described by a characteristic phase function, further discussed below. Most particles in the atmosphere fall in between the two size extremes and require complex calculations to compute scattering properties (Petty, 2006).

Gas molecules fall in the very small range and mostly absorb radiation. Although molecules do scatter radiation, it usually a rather small percentage of the total extinction. Aerosols on the other hand, make up the particles that fall in between the two extremes noted earlier and are relatively much larger than gas molecules. Scattering and absorption properties of aerosols varies by size, shape, concentration and wavelength. Methods applicable to calculating optical scatter of small randomly oriented particles use Rayleigh theory, while those applicable to spheres of arbitrary size use Mie theory (Petty, 2006).

As already introduce, the size of a particle, the CIR, and the wavelength of radiation are major factors when calculating the particle's optical properties. The non-

dimensional size parameter, *x*, is the term used to describe scattering behavior of particles, that is whether Rayleigh, Mie, or geometric theory is appropriate for calculating their scattering properties. The size parameter can be calculated using wavelength, λ, and radius, *r*, of a specific particle.

$$x \equiv \frac{2\pi r}{\lambda} \tag{7}$$

Figure 1 shows the relationship between the scattering behavior, size, and wavelength. When x << 1, the scattering behavior follows the Rayleigh theory, when x ≈ 1, the scattering behavior follows Mie theory, and when x >> 1 the scattering behavior follows geometric scattering patterns.

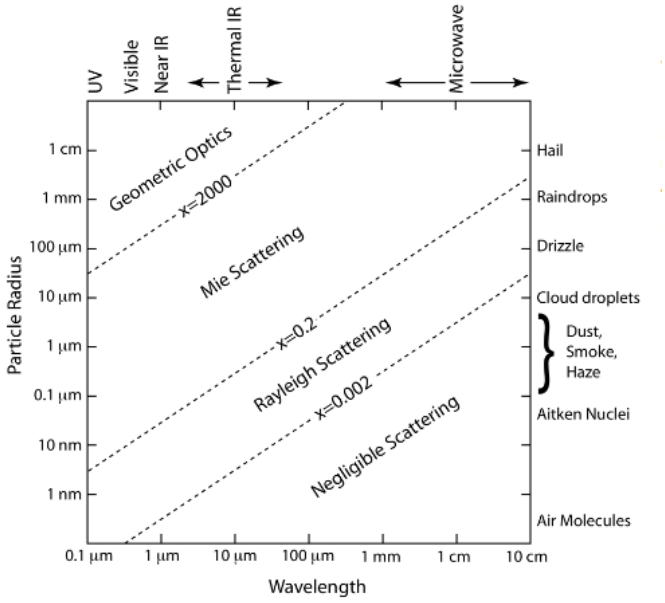

Figure 2. Graphical depiction of the relationship between particle size and radiation wavelength. The diagonal dashed lines describe the scattering behavior for atmospheric particles (Petty, 2006).

Another key property is the relative index of refraction, *m*, expressed as

$$m \equiv \frac{N_2}{N_1}, \tag{8}$$

where N_2 is the CIR of the surrounding medium, and N_1 is that of the particle. These indices, have real and imaginary components, $N = n_r + n_i i$, and N varies with wavelength for all substances. The real component governs the phase speed of EM waves propagating through a medium, while the imaginary part governs absorption. The ability to determine the real and imaginary indices is key to properly characterizing aerosol absorption and their effect on both laser propagation and the atmosphere. Fiorino et al (2012), showed that both the real and imaginary components are partially codependent and can be determined through iteration. Previously it was assumed that the imaginary index can be derived by subtracting Mie-calculated scattering from measured extinction. However, by comparing measured off-axis scattering phase functions to empirically calculated phase function, and varying optical properties, Fiorino et al (2012) was able to show that that assumption was not correct, and develop a method to fully and accurately determine both real and imaginary components of the CIR.

Another important factor in radiative properties of particles is the shape. Considering that aerosols are not spherical, rather randomly oriented shapes, it is common to assume all particles are spherical in most radiative transfer calculations since there is a large number and variety of particle shapes for which to account (Petty, 2006). For non-spherical particles, r represents a radius of a sphere that would have the same surface area of the particle.

As mentioned above, the scattering phase function describes the angular distribution of radiation scattered by particles. The phase functions of real atmospheric particles can be complex and do not have simple mathematical descriptions. This is where the asymmetry parameter can come in handy, and it tells the relative proportion of

photons that are scattered in the forward verses backward directions. The asymmetry parameter can be interpreted as the average value of cos θ for a large number of scattered photons, and can be expressed as

$$g \equiv \frac{1}{4\pi}\int_{4\pi} p(cos\theta)\, cos\Theta d\omega, \tag{9}$$

and

$$-1 \leq g \geq 1. \tag{10}$$

When g > 0 photons are scattered in the forward direction, and when g < 0 photons are scattered in the backward direction. In the case when g = 0, it implies that photons are scattered equally in the forward and backward directions, known as isentropic scattering.

Scattering by gas molecules is called Rayleigh scattering and involves particles much smaller than the wavelength in the visible portion of the EM spectrum. For Rayleigh scattering, intensity is proportional to the fourth power of inverse wavelength (Petty, 2006). The phase function for Rayleigh scattering is quite smooth and perfectly symmetric with respect to forward and backward scattering. This is further expressed in the asymmetry parameter, as $g = 0$ for molecular scattering.

Even the cleanest air found in nature contains both gas molecules and aerosols, which are relatively much larger than gas molecules. Scattering by aerosols does not have as strong of a dependence on wavelength and the scattering phase function for aerosols is not symmetric, but rather exhibits strong forward scattering. Aerosols do not satisfy the Rayleigh criterion, and therefore Mie theory is used in calculating phase functions for these particles. Mie theory involves Maxwell's equations to derive a wave equation for EM radiation in a three-dimensional space. Separable differential equations expressed as infinite series, usually truncated to keep only enough terms to yield a sufficient

approximation, are used to represent the scattering phase function. Mie calculations are dependent on the size parameter, *x*, and the relative index of refraction, *m*. An example of various Mie-derived phase function for various size parameters and an index of refraction of 1.33 is shown in Figure 2. The larger the particle the more terms are required to be kept in the series, and therefore, at some point geometric optics become the preferred method to calculate optical properties (Petty, 2006).

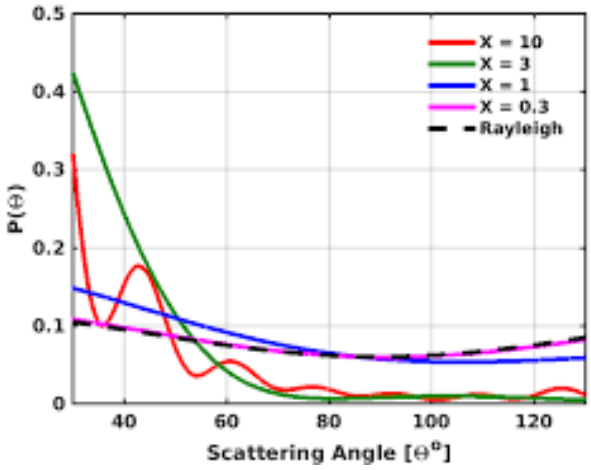

Figure 3. Mie-derived phase functions profiles for a single relative index of refraction value, m = 1.33, and various size parameter values. As x increases, asymmetry and complexity of phase functions changes (Petty, 2006).

2.4 Aerosol Properties and Databases

Aerosols exhibit significant temporal and spatial variations, both in quantity and optical properties. This includes number densities, size distributions, refractive indices, shape, and even distribution with altitude. Additionally, aerosol direct radiative forcing varies with solar elevation and surface albedo (Koepke et al, 1997). In climate assessments, it is desirable to account for these variations within global circulation models. For directed energy applications, access to specific aerosol data for any potential location at any given time is particularly useful. The Global Aerosol Data Set (GADS),

developed by Koepke et al (1997), provides a gridded 5-degrees by 5 degrees worldwide surface aerosol climatology of seasonal number concentrations, and optical properties for different constituents that account for relative humidity variations and multiple EM wavelengths. Furthermore, to make microphysical and optical properties in the solar and terrestrial spectral range of atmospheric particulate matter available and easy to handle in numerical modeling applications, Hess et al (1998) developed the Optical Properties of Aerosols and Clouds (OPAC) software package that incorporates GADS.

Real aerosol profiles in the atmosphere are often a mixture of different components. Aerosol databases, like OPAC and GADS, that incorporate emission data are limited and far from complete. At the time these databases were developed, the characterization techniques made it impossible to make sufficient measurements of aerosol properties suitable for climate modeling (Koepke et al, 1997). Nevertheless, the data provides a useful tool for aerosol research with respect to average conditions at a certain location. In characterizing aerosol degradation to laser propagation, average conditions may not be representative of the actual atmosphere at the time of interest. For example, most fair weather afternoons are characterized by the increase in small particles that are radiatively important, but do not significantly change the mass density (Fiorino et al, 2019). However, OPAC and GADS allows for the possibility to model relevant optical properties of any mixture of aerosols for individual cases, as well as integrate changes in both physical definitions and scatter theory. These datasets were developed to allow for improvement of the data as observation and measurement techniques are expected to improve over time (Koepke et al, 1997 and Hess et al, 1998).

In GADS, aerosol particles are described by 10 main components which are characterized through their size distribution and their wavelength dependent refractive index. These component types are based on both aerosol emissions and formation and removal processes. Typical components include water-soluble (WASO), water-insoluble (INSO), soot (SOOT), sea-salt (SS), mineral (MC), and sulfate solution (SUSO). There are two size classes for salt and four size classes for mineral. Each component in GADS includes microphysical properties and optical parameters as shown in Figure 4 and 5. Microphysical properties include mode radius, r_m, width of the distribution, σ, and density, ρ.

These properties are then used to determine volume, mass, and the size distribution. Optical properties include extinction, scattering, and absorption coefficients, the single scattering albedo, asymmetry parameter, and the phase function. Further explanation of the optical and microphysical properties of each component type can be found in Koepke et al (1997) and Hess et al (1998).

Components of the Global Aerosol Data Set

No.	Aerosol Component	Name	r_m [µm]	σ	ρ [g/cm^3]
1	Water-insoluble	**INSO**	4.71E-1	2.51	2.0
2	Water-soluble	**WASO**	2.12E-2	2.24	1.8
3	Soot	**SOOT**	1.18E-2	2.00	1.0
4	Sea-salt (accumulation mode)	**SSAM**	2.09E-1	2.03	2.2
5	Sea-salt (coarse mode)	**SSCM**	1.75E+0	2.03	2.2
6	Mineral (nucleus mode)	**MINM**	7.00E-2	1.95	2.6
7	Mineral (accumulation mode)	**MIAM**	3.90E-1	2.00	2.6
8	Mineral (coarse mode)	**MICM**	1.90E+0	2.15	2.6
9	Mineral-transported	**MITR**	5.00E-1	2.20	2.6
10	H_2SO_4-Droplets	**SUSO**	6.95E-2	2.03	1.7

Figure 4. Table 1 from Koepke et al (1997). Lists the GADS aerosol components and their microphysical parameters.

Optical Parameters of Aerosol Components GADS						
Aerosol Component	λ = 0.5 μm			λ = 10 μm		
	σ_e^* [m²/g]	ω_0	g	σ_e^* [m²/g]	ω_0	g
INSO	0.21E+0	0.72	0.84	0.18E+0	0.58	0.66
WASO	0.36E+1	0.98	0.68	0.49E-1	0.04	0.16
SOOT	0.11E+2	0.23	0.35	0.35E+0	0.00	0.01
SSAM	0.13E+1	1.00	0.78	0.84E-1	0.49	0.56
SSCM	0.12E+0	1.00	0.82	0.13E+0	0.72	0.87
MINM	0.28E+1	0.95	0.67	0.91E-1	0.09	0.16
MIAM	0.55E+0	0.83	0.76	0.32E+0	0.47	0.38
MICM	0.74E-1	0.62	0.87	0.95E-1	0.52	0.69
MITR	0.26E+0	0.78	0.81	0.24E+0	0.48	0.44
SUSO	0.38E+1	1.00	0.77	0.17E+0	0.05	0.12

Figure 5. Table 4 from Koepke et al (1997). Lists three Mie-calculated optical parameters, mass extinction efficiency (σ_e^*), single scatter albedo (ω_0), and asymmetry factor (g), for GADS aerosol components at 0.5 μm and 10 μm wavelengths.

The radiative properties are calculated by Mie theory at wavelengths between 0.25 and 40 μm, and at 8 different relative humidity values. GADS assumes a lognormal size distribution for each aerosol type at given location, altitude, season, and relative humidity, expressed as

$$\frac{dN(r)}{d(loglog\, r)} = \frac{N}{\sqrt{2\pi} log(\sigma)}\, exp\left(-\frac{1}{2}\left(\frac{loglog\, r - loglog\, r_M}{loglog\, \sigma}\right)^2\right) \qquad (11)$$

where N is the total particle number concentration per unit volume (cm^3), r_M is the mode radius, and σ is the standard deviation to describe the width of the distribution. The total size distribution for the sample is the sum of that of the individual components. This lognormal distribution is evident in nearly all size spectrometer measurements of ambient aerosol particles; an example measurement at JBO is shown in Figure 6.

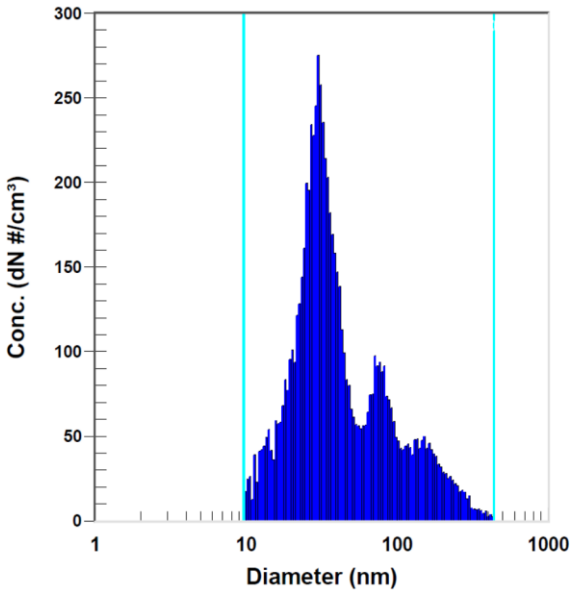

Figure 6. Lognormal size distribution measured by the TSI SMPS.

The CIR varies with wavelength and chemical substance. Rather than individual refractive index values for each type of chemical substance, GADs gives CIR as a bulk property for the component types. This means that real and imaginary CIR values are assumed based on typical internal mixtures of chemical substances for a component type. This assumption is only valid for particles in solution with water but provides a good starting point for average mixtures (Koepke et al, 1997). The spectral dependence of the real and imaginary refractive indices of dry particles is illustrated in Figure 7.

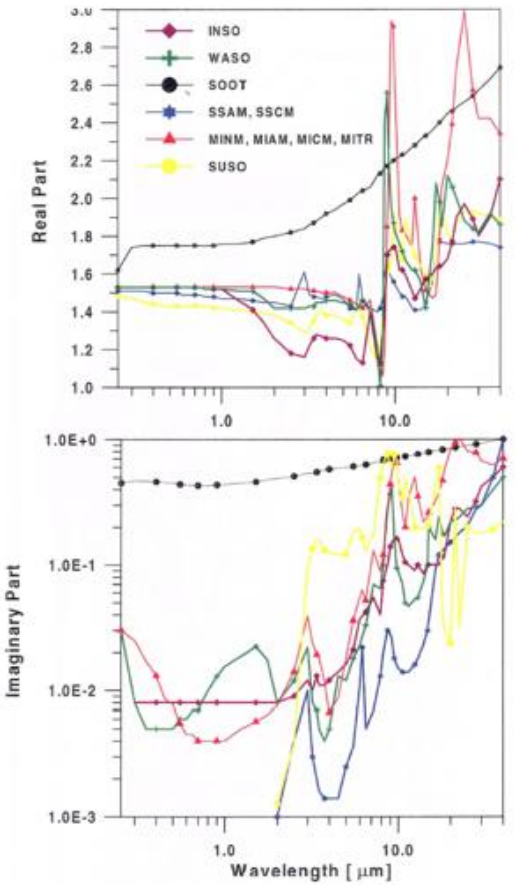

Figure 7. Figure 1 from Koepke et al (1997). Depicts the relationship of real and imaginary complex refractive indices with wavelength for the GADS aerosol components.

Wavelength specific extinction (*E*), scattering (*S*), and absorption (*A*) coefficients can be computed by integrating over the range of particle radii. The single scatter albedo and the asymmetry parameter are obtained as weighted averages of extinction coefficient and scattering coefficient respectively, of the corresponding values for the individual components given by equations (Koepke et al, 1997):

$$\omega_o\ (\lambda) = \sum_i \omega_{oi}(\lambda) \cdot \frac{E_i(\lambda)}{\sum_i E_i(\lambda)} \tag{12}$$

$$g(\lambda) = \sum_i g_i(\lambda)\ \cdot \frac{S_i(\lambda)}{\sum_i S_i(\lambda)} \tag{13}$$

Mie-calculated optical parameters – mass extinction efficiency, single scatter albedo, and asymmetry parameter – at 50% relative humidity as a function of wavelength is plotted in Figure 8. The plots are examples of the complexity of aerosol optical properties discussed in previous sections. The smaller sized particles (WASO, SOOT, and SUSI) decrease in extinction efficiency with increasing wavelength, more prominently in the visible range. All component types, except soot, are weak absorbers in the visible and NIR range but become stronger absorbers at longer wavelengths, which demonstrates that the imaginary refractive index is not constant for a substance. Lastly, it's important to keep in mind that these plots are not necessarily representative of all scenarios within the atmosphere, rather they are average profiles for the main component types within GADS for a particular relative humidity situation.

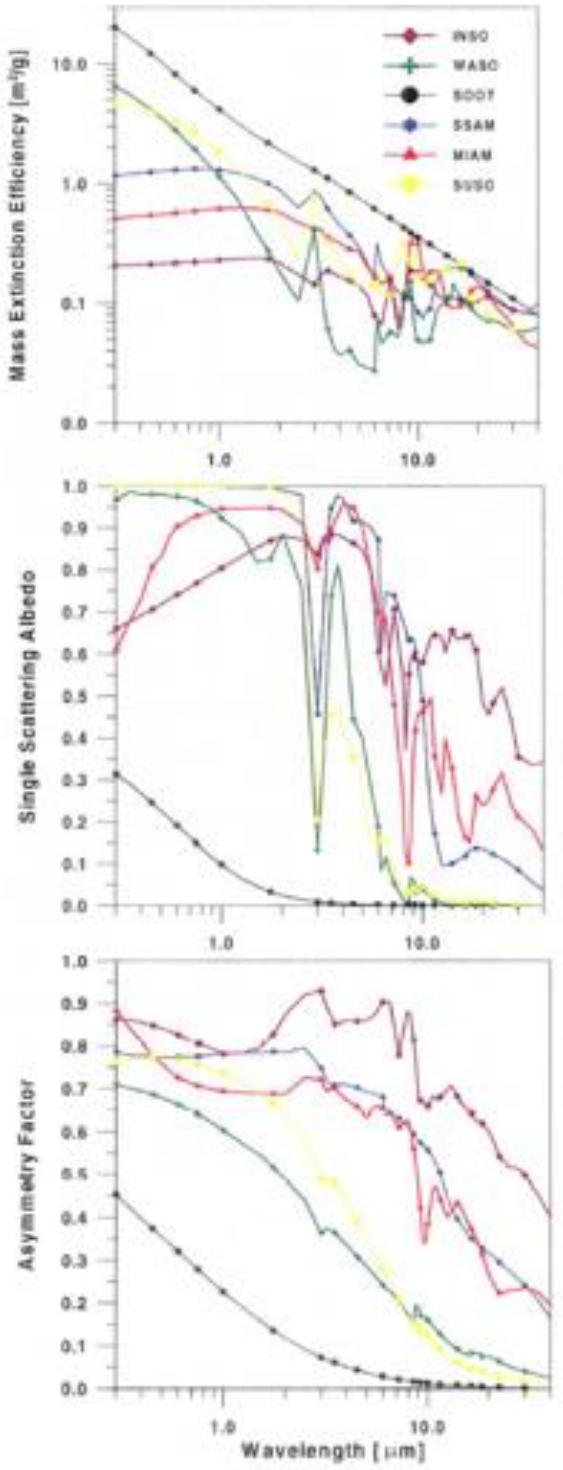

Figure 8. Figure 2 from Koepke et al (1997). Depicts the relationship of three Mie-calculated optical parameters, extinction efficiency (top), single scattering albedo (middle), and asymmetry parameter (bottom) with wavelength for the GADS aerosol components.

III. Methodology

In order to test the hypothesis that measured off-axis backscatter from high energy lasers can be used to determine bulk aerosol absorption, measured and predicted phase function profiles of off-axis scattered laser energy are needed for comparison. Phase functions describe the amount of relative radiation that is scattered in each direction based on gas particle and aerosol mixture. Comparing the difference between measured and predicted phase function provides information on the actual particles present in the air.

Predicted phase functions and off-axis irradiance values are created using HELEEOS and LEEDR modeling packages. The initial proposed method to build measured phase function profiles was to convert raw pixel data from off-axis images of a laser beam, taken with a calibrated visible/SWIR camera, into physical units of energy and relate to a phase angle using geometry calculations. Complications with both the visible camera calibration and laser operation schedule prevented calibrated images from being captured. Therefore, the use of measured irradiance values are not used in the analysis.

An alternate measurement technique, using a G9 Canon digital camera, is chosen in order to qualitatively test the hypothesis. The camera is a CCD type image sensor with a lens aperture that ranges from 7 mm to 44 mm. Rather than irradiance values and a measured phase function profile, changes in intensity, or brightness, in the pixels digital output values are qualitatively compared to predicted scattering irradiance values.

The energy source is a Rayleigh beacon pulse laser with an output wavelength of 527 nm, an exit aperture of 60 cm, an output energy of 8 mJ per pulse, and a pulse

repetition frequency of 200 Hz. In contrast to the longer wavelength lasers used in Haiducek, average power per duty cycle output of the high energy laser used in this research is approximately 1.6 Watts. Laser experiments are conducted during nighttime hours in order to more clearly see and locate the laser beam scatter from the off-axis location, as well as reduce exposure to background light noise.

In order to analyze how aerosol absorption characteristics alter the phase function, several LEEDR-calculated predicted phase function profiles are created using various imaginary index of refraction values. Additionally, to demonstrate the importance of accurately representing the CIR within absorption coefficient derivations, extinction, absorption, and scattering coefficient profiles for 5 and 6 November 2019 are created using measured aerosol data and two different methods of Mie calculations coded in LEEDR.

3.1 Field Measurements

3.1.1 Measured Profiles

Images of the Rayleigh beacon pulse laser beam, described in Chapter 1, are captured at JBO on 5 November 2019. The off-axis observation point is located 20 meters to the northeast (approximately a 45º relative azimuth angle) of the laser platform, and the beam is aimed to the north at a 45º elevation angle (angle from the ground). The laser platform is 3 meters off the ground, while the observations were taken at approximately 1.5 meters off the ground. Because the laser beam is aimed into the sky with no actual target, a target altitude is arbitrarily chosen to be at 100,000 meters to

represent the approximate top of the atmosphere. Using geometry, the length of the beam can be calculated using the following equation:

$$Beam\ Length = \frac{100{,}000}{\sin 45°} \tag{14}$$

Therefore, the length of the beam used in calculation throughout this research is approximately 141,500 meters. The set-up is shown in Figure 9 (not to scale).

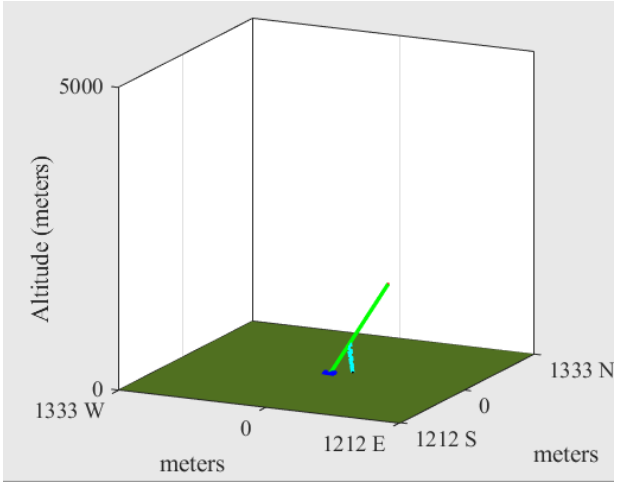

Figure 9. 3-D graphical depiction, created in HELEEOS, of field set-up for the off-axis observation measurements. Due to the very long beam length, and the short distance between the laser platform and the observer, depiction is not to scale.

In order for the data collection to be used, atmospheric scattering must be visible in the images, and it must be possible to determine the laser energy as the source of the scattering. This is possible with the G9 Canon camera by taking images at night when there is very little background noise, and by adjusting to a high exposure setting that enables the camera to capture multiple pulses of the laser beam. This is accomplished by decreasing the shutter speed to 15 seconds and adjusting the aperture value for a smaller lens view. The shutter speed and lens view remain constant for all images, which prevents images of the entire beam from being captured in a single image. Therefore, the length of the beam in each image varies as the viewing angle is adjusted.

Raw digital images of the laser have low contrast making it difficult to identify the laser beam pixels verses background pixels. Therefore, simple image enhancements are applied to view and analyze laser pixels (Figure 10). The images on the left are the raw digital images of three separate sections of the beam, while the images on the right are the corresponding images processed using a contrast enhancement. The enhancement involves several steps. First, the raw image is inverted in that each pixel value is subtracted from the max pixel value. Second, the inverted image is de-hazed, using method described in Lin and Wang (2012). Lastly, the de-hazed image is inverted to reveal the enhanced image.

Figure 10. Off-Axis laser images captured with a G9 Canon camera. The left set of images are raw images of three different sections of the beam (lower, middle, top). The right set of images are processed using a contrast enhancement (twice inverted and dehazed) to make the laser beam easier to view.

In an effort to qualitatively compare to the predicted phase function profiles, it is necessary to relate pixels to physical locations. To accomplish this, geometry relevant to

each pixel is considered relative to the source and observer location as depicted in Figure 11. The location of a pixel along the laser beam path is described relative to the source in the form of distance BD, and relative to the observer in terms of the angles *a* and *d*. In order to determine the distance BD from the angle *a*, or vice versa, the off-axis angle *b* and the distance AB must be known.

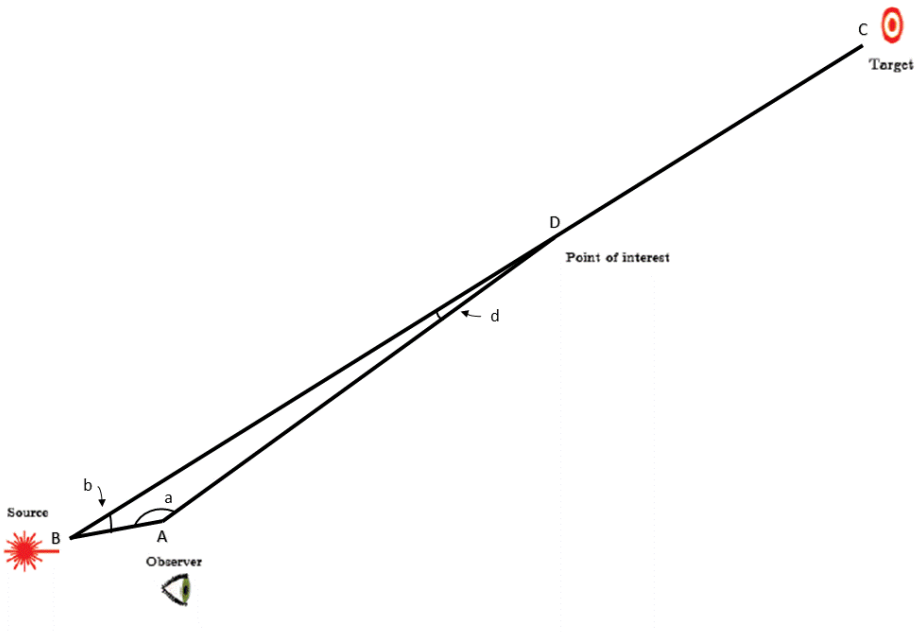

Figure 11. Experiment setup with triangle shown between observer, source, and point of interest along the laser beam path. Geometry relevant to relate pixels to physical location.

The absence of irradiance values prevented complete measured phase function profiles from being created for comparison. Rather, intensity or brightness differences between the digital pixel values are used to qualitatively analyze the change in scattered energy along the beam. With the aim of analyzing laser pixels within each image more easily than the digitally enhanced images (Figure 10), the raw image green channel is scaled to use the full color map, shown in Figure 12. Additionally, in order to ensure brightest pixels are located along the length of the beam, the full scaled image is

manually reviewed using a pixel region tool to identify max pixel index along the laser beam (also shown in Figure 12).

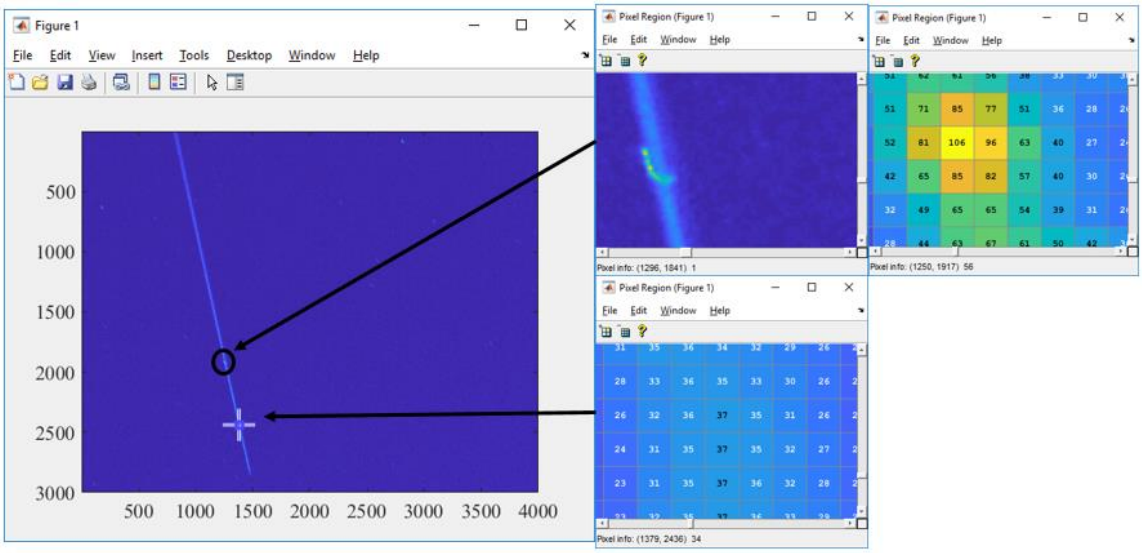

Figure 12. Raw image with green channel scaled to full-range color map (left). Image Processing Tool (right), allows image zoom to see index value assigned to each pixel.

3.1.2 Aerosol Characterization Data

Aerosol characterization information was also gathered at the field site, which included aerosol particle counts, size distributions and aerosol absorption estimates. Aerosol data was gathered using two different condensation particle counter (CPC) devices, a Scanning Mobility Particle Sizer (SMPS) spectrometer, and a continuous light absorption photometer (CLAP). The purpose of collecting particle counts and size distributions was to scale the GADS climatology surface aerosol concentrations within HELEEOS and LEEDR, and use the data to derive scattering and absorption profiles from extinction measurements. The purpose of collecting aerosol absorption values was to compare aerosol absorption profiles to that computed with LEEDR.

The aerosol collection devices were setup in a temperature-controlled enclosure located 3 meters off the ground, with a vertical stack attached to the side of enclosure to pull in ambient air. This collection occurred from October to December 2019.

3.1.2 1 Number Concentrations and Size Distributions

Number concentrations were measured directly using an Aerosol Dynamics Inc. Moderated Aerosol Growth with Internal water Cycling (MAGIC) CPC. A TSI, Inc. CPC is employed in the SMPS. As such, the TSI Inc. CPC does not directly produce number concentration data as the MAGIC does, rather total concentrations are inferred by aggregating size - number concentrations (i.e. summing number concentrations in each of the size bins) measured by SMPS.

The MAGIC is capable of sampling particles with diameters ranging from 5 nm through 2500 nm. The MAGIC was used to provide continuous higher resolution number concentration measurements and to identify diurnal trends in aerosol concentrations at a higher temporal resolution. This information can be an important factor to consider when deriving absorption properties using measurements and comparing to derived absorption properties using a model that relies on climatological data.

The SMPS is capable of sampling particles with diameters ranging from 2.5 nm through 1000 nm. The device is not capable of capturing the entire size spectrum. This is because the size window is limited by the configuration of SMPS components, such as the Differential Mobility Analyzer (DMA) and flow rates impactor sizes. Multiple SMPS and DMA configurations would be required to capture particles across the full size spectrum; however, that was not feasible at the field site. Therefore the device was configured to measure particles ranging from 12.86 nm through 673.17 nm based on the

desire to capture as many big particles without missing the size info associated with nano particles.

SMPS mass densities and number concentration profiles from the data collection field site is shown in Figure 13. The SMPS provided critical size number concentration data needed for correction of aerosol absorption data collected by equipment loaned to AFIT by NOAA and described in the following section.

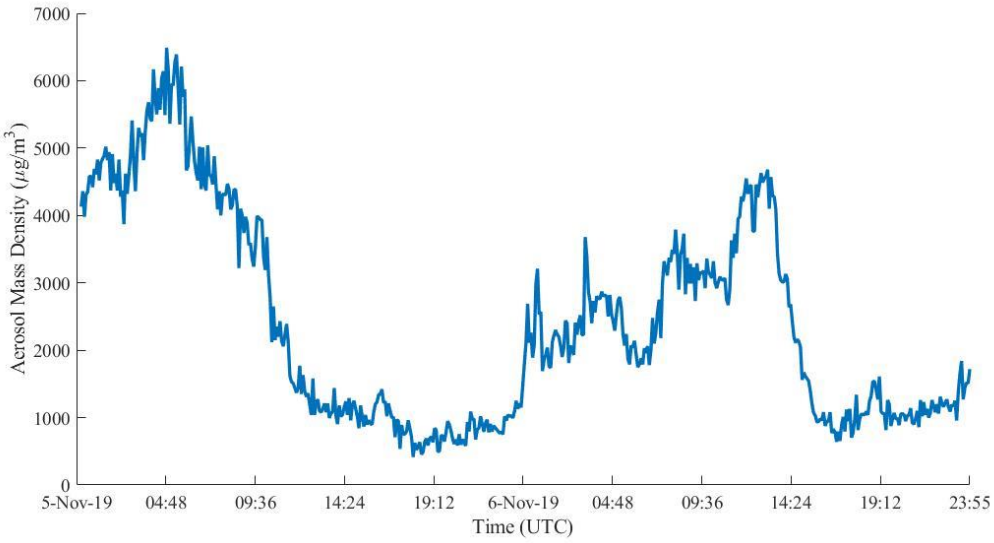

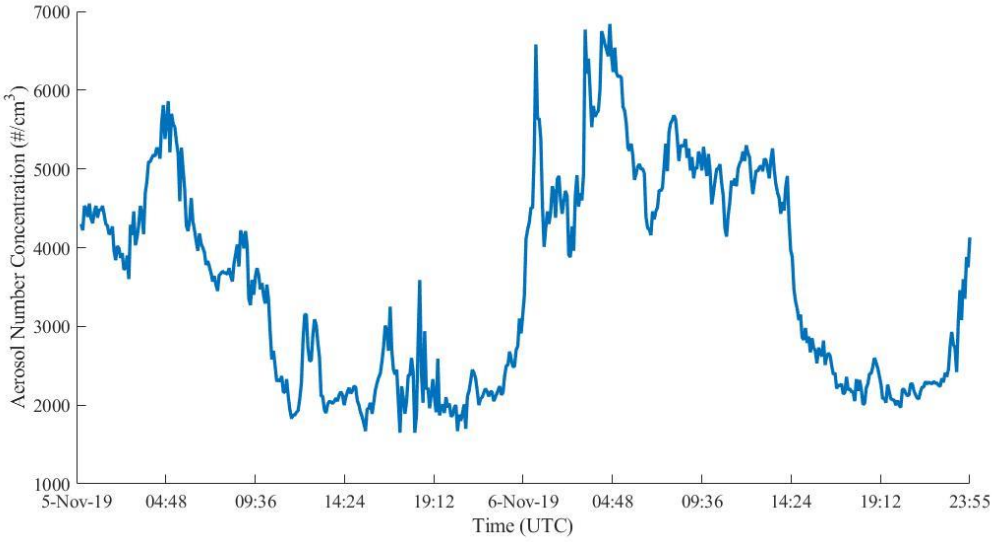

Figure 13. Mass densities (top) and number concentrations (bottom) for 5 and 6 Nov 19. Data was collected with the TSI Inc. Electrostatic Classifier and SMPS with samples recorded every 5 minutes.

3.1.2.2 Absorption Estimates

Absorption estimates were collected using the National Oceanic and Atmospheric Association (NOAA) CLAP device. The CLAP measures the change in light transmission through a filter on which particles are collected, and derives absorption as the difference between light extinction and light scattering of suspended particles, which includes both aerosols and gas molecules. Derivations require either size distribution data to infer aerosol scatter coefficient via Mie scatter calculations, or directly measured aerosol scatter coefficients using a nephelometer. A nephelometer was not available, so the aerosol scatter coefficients were calculated using the size distribution data collected with the TSI Inc. SMPS. Instrument calibration and absorption estimate processes used with this device are detailed in Bond et al (2010).

3.2 Predicted Phase Functions

Predicted phase functions are calculated using the previously discussed off-axis scattering algorithm, and both LEEDR and HELEEOS modeling packages. The field measurement geometry parameters and laser properties are input into HELEEOS to produce scattered irradiance values for each segment of the beam. The same field measurement parameters are then input into LEEDR to produce the predicted phase functions.

Worldwide seasonal, diurnal, and geographical spatial-temporal variation in meteorological parameters in HELEEOS and LEEDR is organized into probability density function using the Extreme and Percentile Environmental Reference Tables (ExPERT) database. Wright-Patterson Air Force Base (WPAFB) is one of the ExPERT sites, while JBO is not. JBO is located approximately 15 miles east of WPAFB, therefore the WPAFB ExPERT data is considered representative of JBO. Additionally, aerosol data is provided from GADS and scaled based on CPC measurements when they significantly differed from seasonal climatology values.

HELEEOS and LEEDR allows the user to input surface conditions, rather than using climatological data. Specifically, surface pressure, air temperature, dew point temperature, and relative humidity are recorded every 30 minutes using automated weather observation equipment located at JBO, averaged over the entire image collection period, and input into both model packages.

The laser platform, target, and observer parameters used in the model calculations are the same as those described in Chapter 1 and the above field measurement section. In order to have predicted phase function profiles that are comparable to measured data, the

model needs to use as much of the same parameters as possible. The user defined input used in both HELEEOS and LEEDR are listed in Appendix A.

3.2.1 HELEEOS

HELEEOS allows the user to define geometry parameters described in the field measurement section, as well as laser properties such as wave type, power output, wavelength, optical focus and transmit (exit aperture) settings, and field of view (FOV) specifics.

Laser wavelength, optical focus, and transmit settings match those described in Chapter 1. It is assumed that a continuous wave laser of power equal to the average power propagated by that of the Rayleigh beacon pulsed laser—available for this research—would provide reasonable insight on the relative magnitude of scattered irradiance. As such, the average output power of the laser (1.6 W), is found by multiplying the pulse repetition frequency (200 Hz) by the energy per pulse (7.98 mJ).

In order to calculate scattered irradiance values at the observation point, the model requires observer FOV parameters to be specified. The observer parameters used in the HELEEOS model are chosen to be representative of a human eye, or a camera, viewing the laser beam from an off-axis location. An angular focusing type FOV is chosen with a $\pm 0.4^{o}$ range so that further down the beam path would result in a longer section of the beam being viewed, as occurs with the human eye.

HELEEOS provides several output values, but the only one of interest in this research is the observer irradiance, that is the amount of irradiance scattered from a specified section of the beam to the off-axis observation point. HELEEOS off-axis scattering model requires a specific point along the beam to be selected in order to

retrieve the scattered irradiance value toward the observer. Several points along the full length of the beam are input into the model in order to retrieve enough data to analyze how scattering changes along the beam path.

3.2.2 LEEDR

LEEDR allows the user to define geometry parameters described in section 3.1, just like in HELEEOS, but additional required parameters include path resolution and path type. The path resolution--defines the number of layers and length of each section of the beam--is set to 283 layers, each 500 meters long. This path resolution is chosen with the nighttime boundary layer height (500 meters) in mind. The path type describes the path of the beam, which in this research is a slant path to represent a beam that is aimed into the sky at an angle.

LEEDR is coded to account for the overall aerosol concentrations as defined in GADS for the user selected location. For WPAFB that includes water soluble, soot, and water soluble aerosols. LEEDR also allows for those values to be adjusted based on in situ observations that vary from the climatological database. However, GADS winter aerosol concentrations values, coinciding with the season the ambient outdoor measurements are collected, are used for the predicted phase function calculations presented in this research rather than aerosol data measured at JBO during image collection. Without measured phase functions to be compared to predicted phase functions, using in situ observation versus GADS is not an important factor.

Additionally, LEEDR accounts for the different index of refraction values of each of the different aerosol components. This value impacts the aerosol absorption values calculated within the model, and to isolate that impact of phase function profiles on

absorption, the index of refraction is held constant within each iteration regardless of the aerosol mix. The aerosol index of refraction is coded to be 1.53-0.010i, which is ammonium sulfate plus an arbitrary absorbing value. In each separate iteration the real component—governs scatter—is held constant but the imaginary component—governs absorption—is varied. The additional values for the imaginary component include 0.001i, 0.006i (GADS), 0.050i, 0.100i, 0.400i (soot), and are chosen to capture the full spectrum of common imaginary index values seen in local aerosol components.

3.3 Extinction, Absorption, and Scattering Coefficient Calculations

In an effort to demonstrate the importance of accurately representing the CIR within absorption coefficient derivations, extinction, absorption, and scattering coefficient profiles for 5 and 6 November 2019 are derived using two different methods of Mie calculations coded in LEEDR. Additionally, absorption data collected using the CLAP device, as described in section 3.1.2.2, is also presented in order to compare the data to the LEEDR-derived absorption values.

The first LEEDR calculation method holds the CIR constant, using the same ammonium sulfate plus an arbitrary absorbing value (1.53-0.010i) described for the phase functions profiles. The second method is the standard LEEDR code which accounts for the different index of refraction values of each aerosol component in the mixture.

Rather than the GADS defined aerosol concentrations, measured values collected with the SMPS at the field site (JBO) are used to calculate the extinction, absorption, and scattering coefficient values. The numerical code requires the user to input surface conditions, specifically, aerosol number concentration, surface temperature, dew point, and pressure. The SMPS recorded size distributions and number concentrations every 5

minutes, while the automated weather observation equipment located at the field site, recorded surface weather conditions every 30 minutes. In order to calculate over the entire 2-day period, both sets of data are meshed, which interpolated the surface weather conditions to match the total number of aerosol concentration samples. Single extinction, absorption, and scattering coefficients are also calculated for the day and time of laser image collection. Image collection occurred over 2-hour period, 0730-0930L, therefore surface conditions and aerosol number concentrations are averaged over the same 2-hour period in order to be more representative. The values are 2,180 parts/cm^3, 42º F, 31º F, and 1024 mb.

Additionally, the model allows the user to customize the aerosol mixture. However, the GADS aerosol mixture is used in the extinction, absorption, and scattering coefficient calculations presented in this research. For winter season at WPAFB, the total GADS aerosol surface number concentration is 26000.5 per cm^3. The aerosol component break down includes 0.5 parts/cm^3 non-water soluble, 15,000 part/cm^3 soot, and 11,000 parts/cm^3 water soluble.

IV. Results

4.1 Off-Axis Laser Images

The inability to derive precise, quantitative irradiance data resulted in a less rigorous quantitative analysis of the laser beam images. Pixel information is plotted on the image to show the pixel location, index value, and actual raw digital RGB value for several points along the beam and in the background (Figure 14a).

Images are displayed with green channel scaled to a full color map in order to view the brightness values along the beam. Brightness values increase along the length of

the beam, indicating that greater scatter irradiance is seen at greater backscatter angles. This is to be expected at greater viewing angles (viewing further out along the beam) as larger sections of the beam are being observed, and thus more aggregate scatter is reflected back to the observer. Additionally, analysis of the rate of increase of 10 equally spaced pixels along the beam show that the increase in backscattered irradiance is greater for the lower portion of the beam than the top portion of the beam (Figure 14b).

Figure 14a. Image of the upper portion of the beam taken with a G9 Canon digital camera. Pixel index and location are plotted along the beam to show the increase in brightness values at larger phase angles, indicating an increase in scattered irradiance.

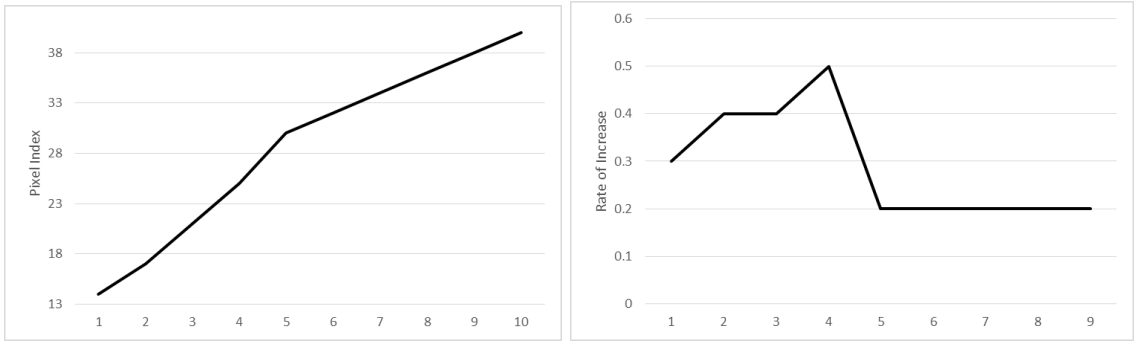

Figure 14b. Rate of change depiction of 10 equally spaced pixels, in ascending order, along the length of the beam and plotted two different ways; pixel index value verses beam location (left), and rate of increase verses beam location (right).

4.2 Predicted Observer Irradiance

HELEEOS-derived observer irradiance values are computed and retrieved to compare to the scattered irradiance pattern along the length of the beam observed in the laser beam images. Figure 15 shows an example of the HELEEOS output. Since the same ±0.4 degree angular view is used in each iteration, the length of the section of the beam observed increases the further away from the start of the beam.

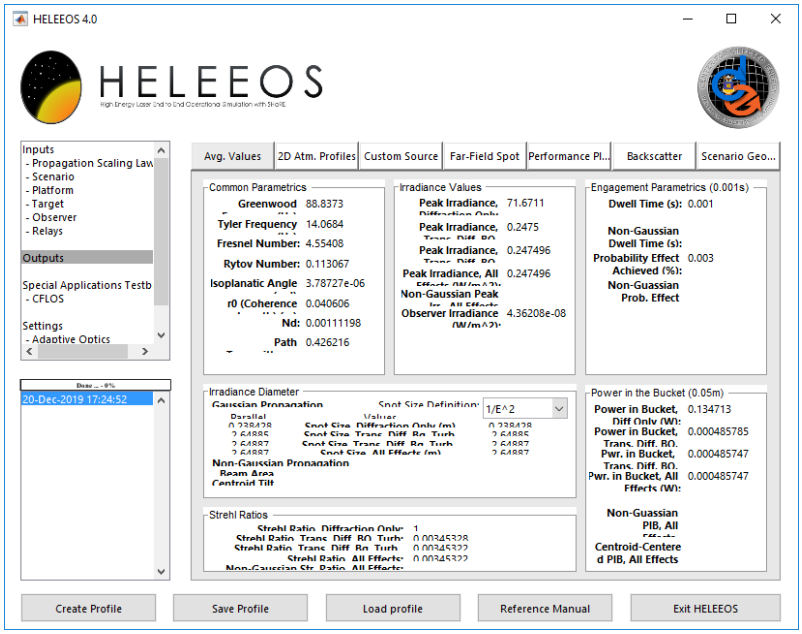

Figure 15. Example of HELEEOS output using the off-axis algorithm. Observer irradiance can be found in the center box titled irradiance values.

Several points along the beam are input into the model and each observer irradiance value is plotted to show the change in scattered irradiance that reaches the observation point along the beam path (Figure 16). The model predicts an increase in irradiance at larger phase angles, which are backward scatter angles. It is important to note that, the increase in scattered irradiance shown in the following figures does not suggest that more irradiance is scattered from any particular point, but rather that larger

sections of the beam are being observed at further distances, resulting in more aggregate backscattered irradiance.

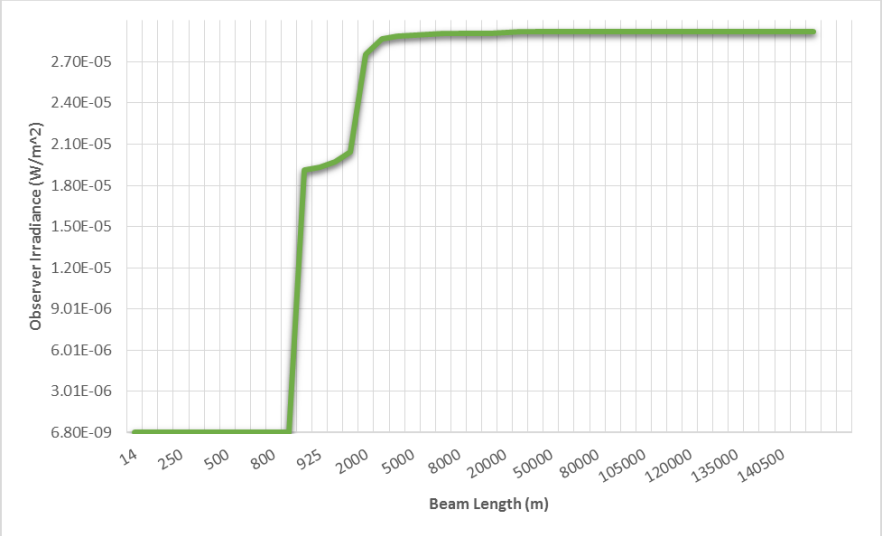

Figure 16. HELEEOS-calculated observer irradiance along the entire length of the beam.

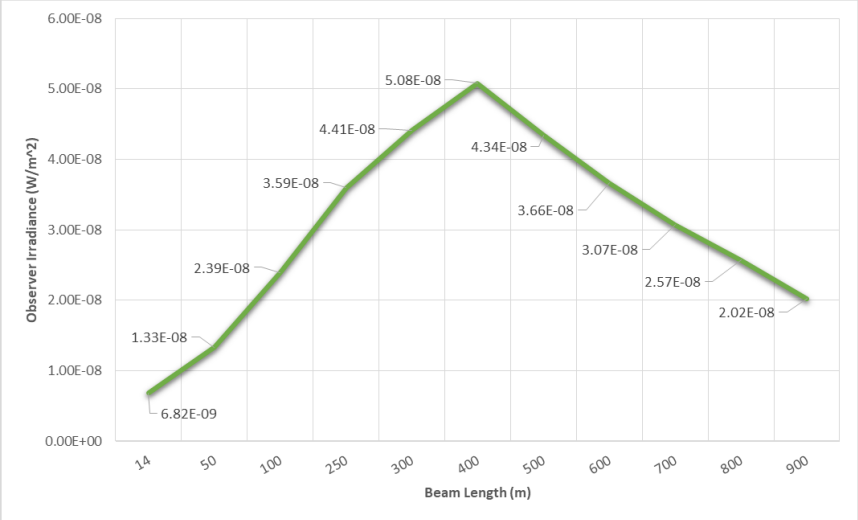

Figure 17. HELEEOS-calculated observer irradiance along the first 1000 m of the beam.

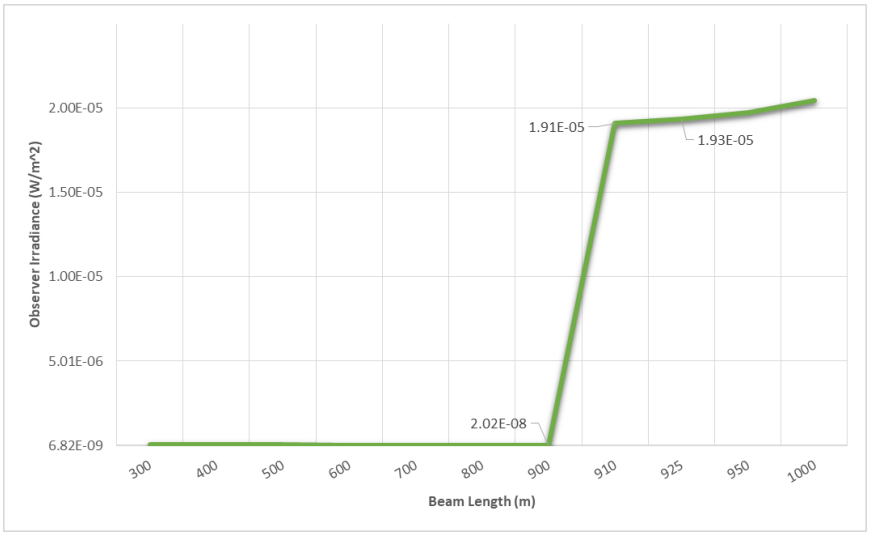

Figure 18. HELEEOS-calculated observer irradiance from 300 m to 1,000 m.

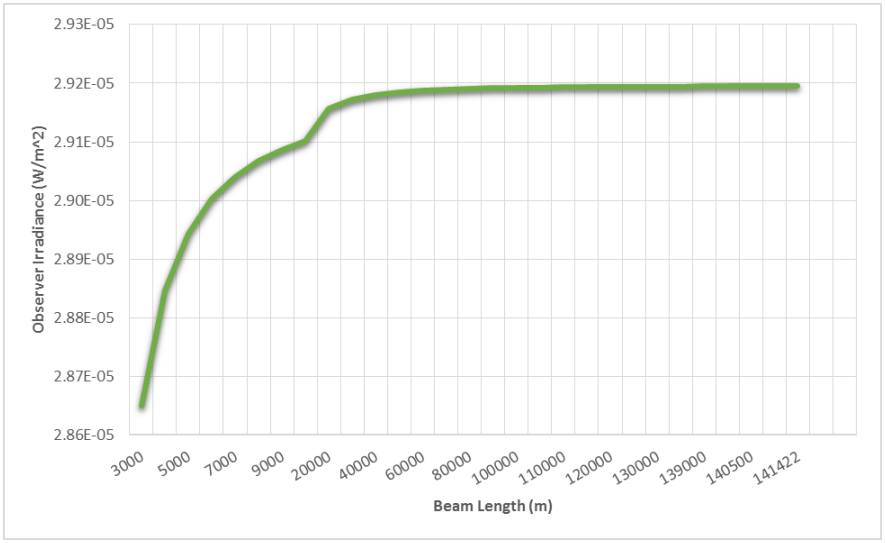

Figure 19. HELEEOS-calculated observer irradiance from 3,000 m to 141,500 m

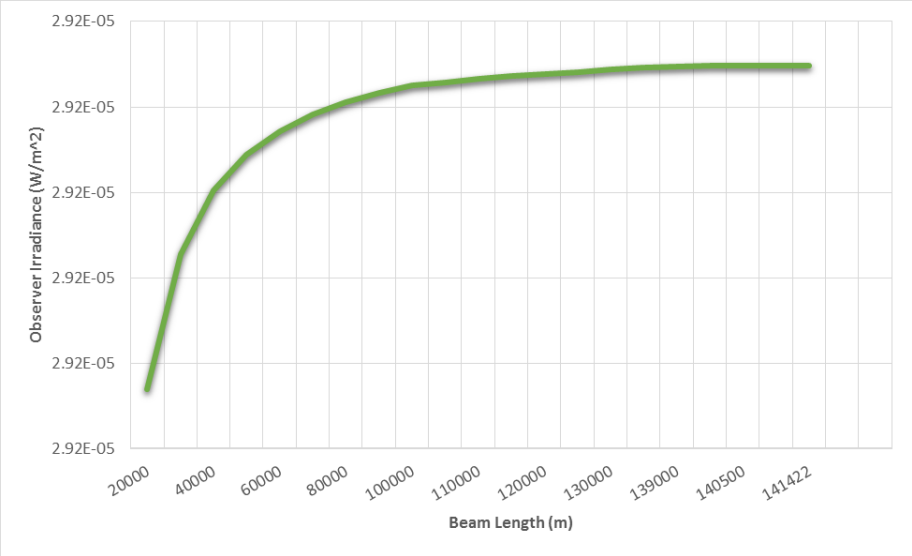

Figure 20. HELEEOS-calculated observer irradiance from 20,000 m to 141,500 m

Zooming in on different sections of the beam (Figures 18-20) show a similar overall pattern observed in Figure 16, which is a rapid increase followed by a slow and steady increase. The last 50,000 meters of the beam reveals a very small increases in observer irradiance with upward viewing angle adjustments. This is due to the fact that at very small changes in viewing angle, a camera lens would be viewing almost the same sections of the beam.

Closer analysis of the HELEEOS-predicted observer irradiance verses beam length graphs (Figure 16), reveals two sharp peaks in observer irradiance. One at 400 meters (Figure 17), and the other at 900 meters (Figure 18). A best guess of these features would be a boundary layer or some sort of inversion that would cause a notable change in aerosol particle number concentration or mass densities at those altitudes. These patterns are not observed in the laser image pixel analysis because background light noise near surface made it impossible to differentiate between laser pixels and background pixels at these low levels.

Using simple geometry relations, as depicted in section 3.1.1 for determining beam length, the altitude of both peaks can be determined given the beam length. The first sharp peak (400m) in scattering is calculated to be occurring at a height of approximately 282 meters, while the second sharp peak (900m) is calculated to be occurring at 37 meters. LEEDR and HELEEOS assumes the boundary layer height at night to occur at 500 meters, therefore the sharp increase at the 900 meter mark is likely an impact of the boundary layer.

It is important to note that these observer irradiance values are model derived calculations that take into account model predicted atmospheric features and variations with altitude. Even though conclusions on the cause are drawn, these same features are not able to be observed in the visible images captured for this research.

4.3 Predicted Scattering Phase Functions

Even though measured phase function profiles are not used in this research, a look at the LEEDR-derived predicted phase functions described in Chapter 3 can provide useful information about backward scattering angles and absorption properties. Each imaginary index value used to derive the phase functions, results in a slightly differing path extinction and attenuation values output by LEEDR (Figure 21). The multiple phase function profiles computed in LEEDR (Figure 22) depict how absorption properties changes the shape of the scattering phase function at backward angles.

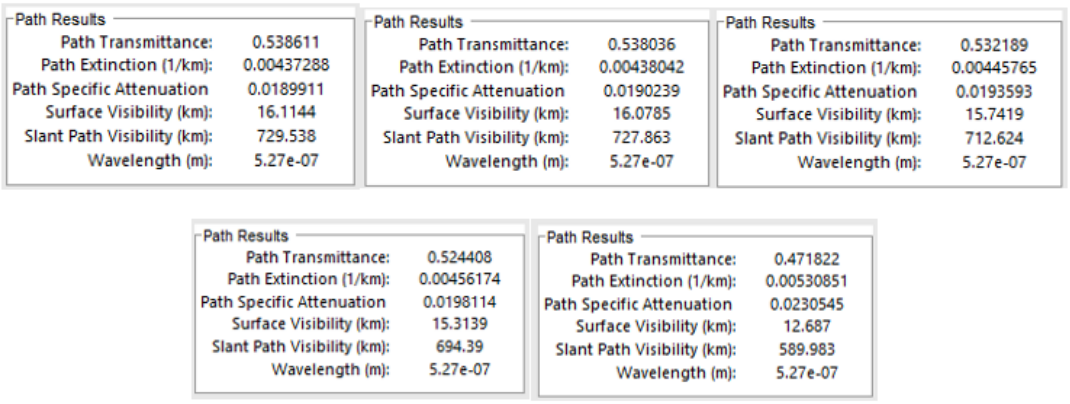

Figure 21. Resultant path transmittance and extinction calculated with various imaginary index values; 0.001i (top left), 0.006i (top middle), 0.050i (top right), 0.100i (bottom left), 0.400i (bottom right).

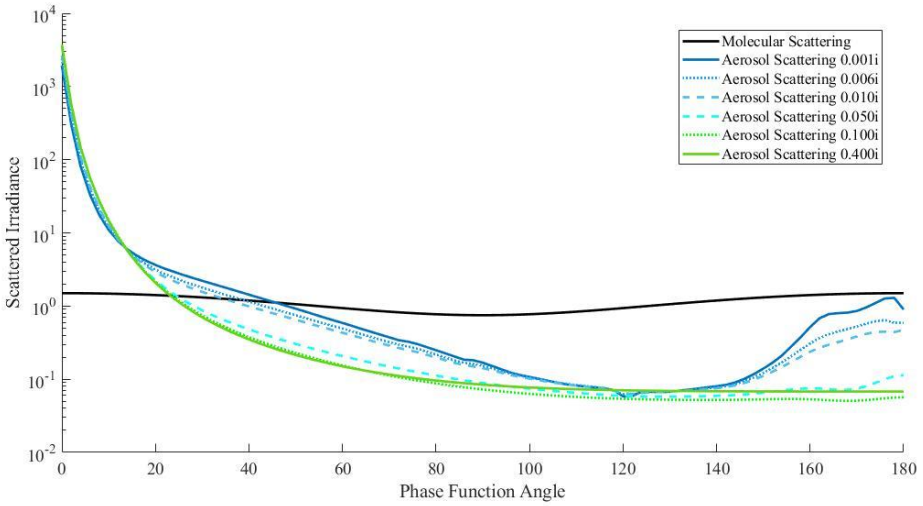

Figure 22. Multiple LEEDR-derived predicted phase function profiles. The black solid line represents molecular (Rayleigh) scattering, while the blue and green lines are the different aerosol scattering (Mie) phase functions resulting from various imaginary index values.

4.4 Extinction, Absorption, and Scattering

LEEDR-derived extinction, absorption, and scattering coefficient profiles for both calculation methods described in Chapter 3 are shown in Figure 23. On 5 and 6 November, both methods result with scattering as the dominate cause of extinction, and

absorption as only a fraction of the total extinction. At first glance, the two methods appear to have the similar results but further investigation reveals that is not the case.

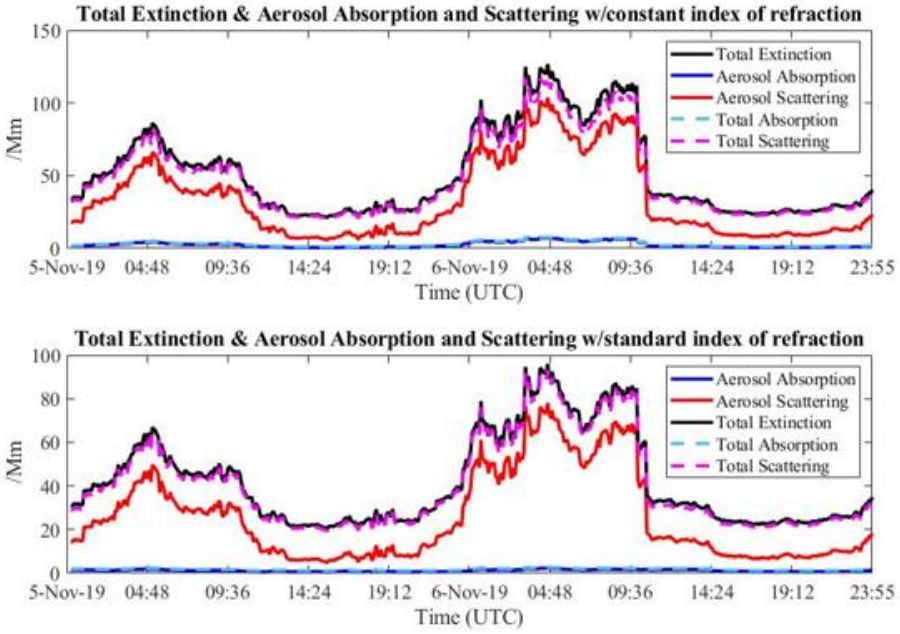

Figure 23. LEEDR-calculated extinction profiles with the CIR held constant (top), and accounting for different index of refraction values of each aerosol component in the mixture (bottom). Solid blue and red lines represent absorption and scattering (respectfully) from aerosols only, while the dashed line represent that resulting from both molecular and aerosol particles.

The difference between the two calculation methods for extinction, scattering, and absorption coefficients (respectively) is shown in Figure 24-26. Both calculation methods result in similar diurnal patterns, but the order of magnitude varies. That is that the constant imaginary refractive index profiles is anywhere from approximately 2-20 parts/Mm greater than the standard index of refraction profiles. The 12-24 UTC (06-18L) timeframe have close agreement in the magnitude, while the 00-12 UTC (18-06L) have a large disagreement in magnitude. This is also the timeframe where there was a measured increase in both aerosol mass densities and number concentrations

(Figure 13). Scattering values during the 00-12 UTC values were up to 20 parts/Mm larger, and absorption values for the same time frame where up to 6 parts/Mm larger using a constant index of refraction calculation.

Holding the index of refraction constant at the ammonium sulfate plus an arbitrary absorbing value (1.53-0.010i), results in overall higher absorption and scattering compared to the standard method used in LEEDR. This can be explained by the fact that the standard method accounts for the smaller soot particles while the fixed method (constant index of refraction) only accounts for the ammonium sulfate particles. Even though soot particles have relatively high absorption rate, they have a much smaller cross section compared to the sulfate particles. These soot properties result in less absorption and scattering when accounted for in the Mie calculations. The fixed method handicaps the effect of soot particles and results in more absorption and scattering because the same number concentration is used in both calculation methods.

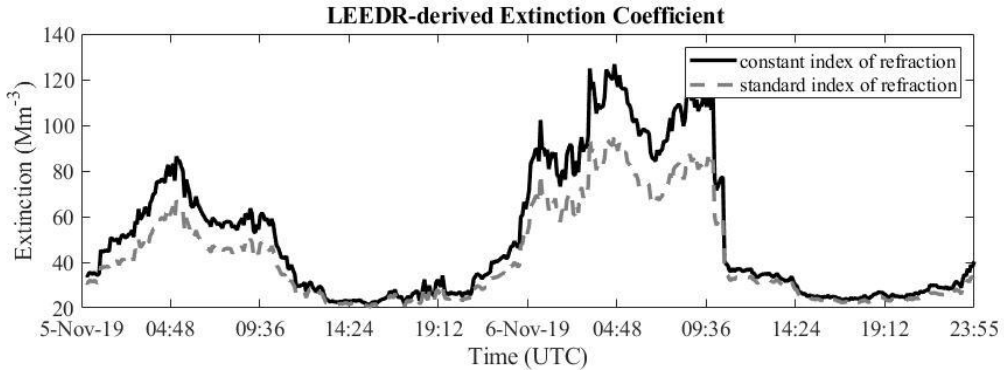

Figure 24. LEEDR-derived total extinction profiles for 5 and 6 Nov 2019. The black solid line represents extinction calculated using a constant index of refraction regardless of aerosol mixture components, and the dashed gray line represents extinction calculation that accounts for all index of refraction values of each aerosol component in the mixture.

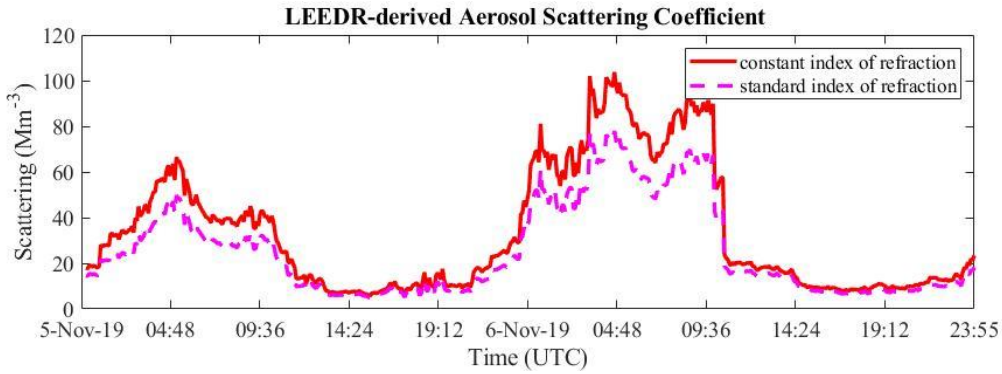

Figure 25. LEEDR-derived aerosol scattering profiles for 5 and 6 Nov 2019. The solid red line represent scattering calculated using a constant index of refraction regardless of aerosol mixture components, and the dashed pink lines represent scattering calculations that accounts for all index of refraction values of each aerosol component in the mixture.

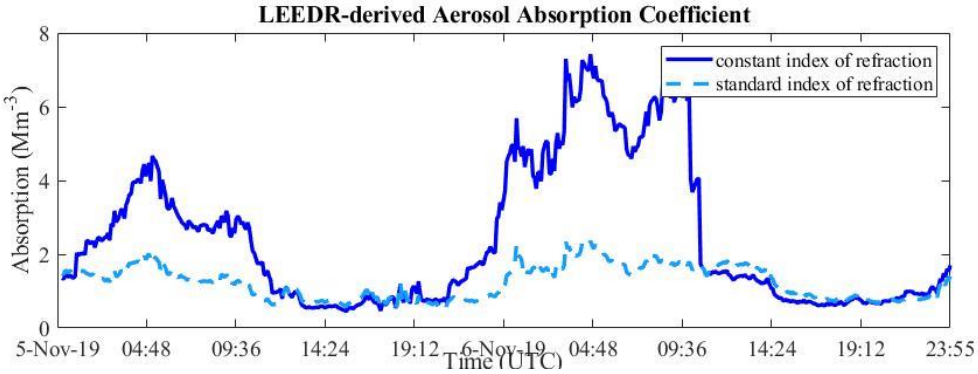

Figure 26. LEEDR-derived aerosol absorption profiles for 5 and 6 Nov 2019. The solid blue line represent absorption calculated using a constant index of refraction regardless of aerosol mixture components, and the dashed blue lines represent absorption calculations that accounts for all index of refraction values of each aerosol component in the mixture.

CLAP absorption data compared to LEEDR-derived absorption values (Figure 27) reveals that LEEDR is capable of profiling aerosol absorption to a similar degree as the CLAP device. The fixed index of refraction calculation method (solid blue line in Figure 27) is comparable to the CLAP absorption data (dotted gray line in Figure 27) on 5 November, but the standard calculation method (dashed light blue line in Figure 27) is comparable to the CLAP absorption data on 6 November. This likely has something to do with the measured increase in both aerosol mass densities and number concentrations

(Figure 13), but it is difficult to fully qualify without detailed information on the aerosol components present at the time of measurement.

LEEDR calculation method requires only a simple number concentration input collected by a single CPC, compared to the more complex CLAP measurement that requires at least one additional measurement device (usually SMPS or a nephelometer) to correct for aerosol scatter. The extinction, scattering, and absorption coefficient results presented here suggest that LEEDR, with a number concentration measurement, can be used as an alternate method of estimating absorption.

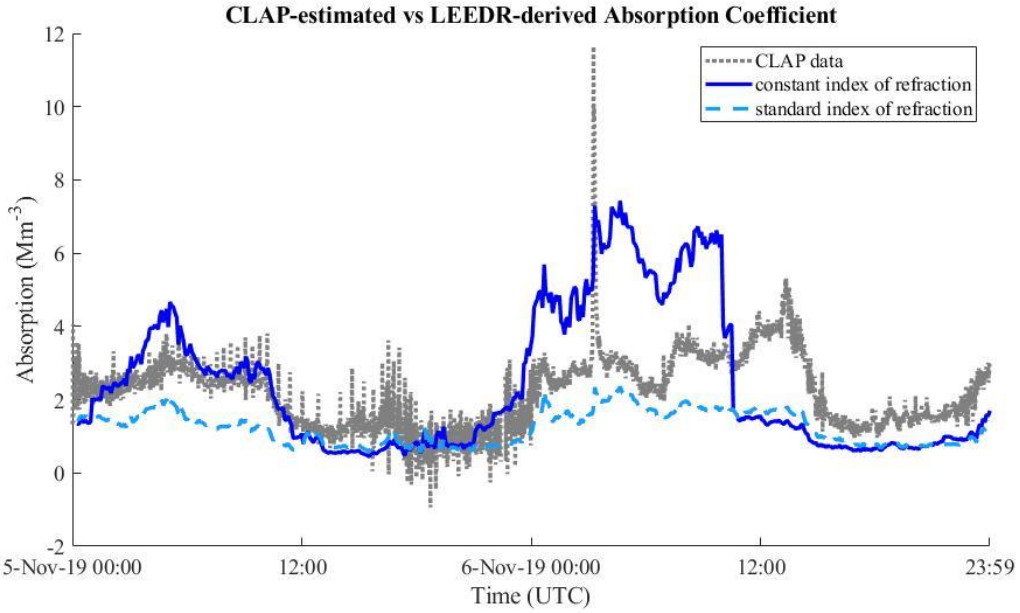

Figure 27. LEEDR-derived aerosol absorption coefficient profile, as depicted in Figure 26, and CLAP-estimated absorption coefficient profile for 5 and 6 Nov. The dotted gray line represents CLAP absorption data.

V. Conclusions and Recommendations

5.1 Conclusions

The tests and evaluations conducted in this research show qualitative agreement between HELEEOS-calculated off-axis observer irradiance and the off-axis field images.

That is, that scattering irradiance increase along the length of the beam, and that there is more scatter in the backward direction. Unfortunately, the lack of a calibrated camera prevented measured irradiance values from being converted from raw pixel data, and thus measured bulk absorption values from being derived. However, at the very least the matching pattern of increasing pixel index brightness (images), and the increasing observer irradiance values (HELEEOS-predicted) shows that original proposed method to determine bulk absorption properties may be possible.

Although there were no measured phase function profiles to compare to the predicted phase function profiles, analysis of backscattering angles of the phase function could be conducted by varying absorption properties in the calculations. Variations in the CIR specifically resulted in changes in the shape of the phase function, notably at backward phase angles. Additionally, scattering and absorption calculations revealed that absorption properties and how they are accounted for can have a major impact in an accurate extinction value, especially during times of higher variation of mass densities and number concentration.

Given the qualitative results from both the off-axis observer irradiance analysis and the phase function comparisons, a major takeaway is that the backscattering portion of scattering phase function offers significant information about aerosol optical properties for off-axis laser energy analysis.

Even though a complete technique, described in Chapter 1, was not fully develop and presented in this research, the results lay the groundwork for future research on using off-axis laser backscatter to determine bulk absorption. Before the technique can be considered fully developed, quantitative data would need to show that scattered

irradiance and a phase function can be accurately measured and derived with a calibrated camera and the LEEDR model.

5.2 Future Work

An obvious next step is to quantitatively test the method using a calibrated high-resolution camera as proposed in Chapter 1. In addition to that, multiple geometry set-ups, allowing for different off-axis angles, and laser power and wavelength variations should be tested against the method. Furthermore, this method of determining bulk aerosol absorption properties can pave the way for improved data assimilation and aerosol loading within NWP by allowing for more accurate local and regional aerosol characterization information. Additionally, in the interest of continued progress in aerosol absorption research, the qualitative findings in this research could be expanded to on-axis HEL spot measurement tests involving thermal blooming displacement and distortion.

The findings in this research, specifically the absorption coefficient profiles presented in section 4.4, suggest that there is a worthy area of study related to climate change research. A general assumption is that soot particles are the cause for an increase in bulk absorption from aerosols, but the three profiles shown in Figure 27 suggest that soot results in lower overall bulk absorption for a constant number concentration.

Appendix A. HELEEOS and LEEDR inputs

A.1. HELEEOS

The HELEEOS settings given here are used for all iteration runs in this projects. Settings are input based on the conditions under which the field images are taken. Not all input sections and tabs are used. For example, default settings are used for clouds and rain, which are no clouds or rain, because laser field operation and images were conducted on clear nights. For any input section or tab not mentioned here, default settings are used.

A.1.1 Propagation Scaling

Propagation Scaling: Gaussian

A.1.2 Scenario

A.1.2.1 Location tab

Latitude: 39.83

Longitude: -84.05

ExPERT Site: DAYTON/WRIGHT-PATTERSON

A.1.2.2 Atmosphere tab

Database: ExPERT

Season: Winter

Time of Day: 00-03

RH Bin Percentile: 50

Aerosols: GADS; Multiplier: 1

A.1.2.3 Ground Level tab

Pressure (mb): 1024

Air Temperature (F): 38

Relative Humidity (%): 83

A.1.3 Platform

A.1.3.1 Geometry tab

Altitude (m): 3

Distance to next Object (m): 141,500

Relative Azimuth to next Object: 0

A.1.3.2 Laser tab

Wave Type: Continuous

Power (W): 1.6

Laser Wavelength: User Wavelength

User Wavelength: 0.527e-6

Laser Source: Top Hat

A.1.3.3 Optics tab

Focus Settings: Default

Relative Obscurant: 0.1

Exit Aperture Diameter (m): 0.6

Beam Quality: 1

Wave front Error (waves): 0

Total System RMS Jitter (rad): 0

Adaptive Optics: None

AO Effect: None

A.1.4 Target

A.1.4.1 Geometry tab

Altitude (m): 100,000

A.1.5 Observer

A.1.5.1 Geometry tab

Enable Observer: checked

Altitude (m): 1.5

Distance to next Object (m): 20

Relative Azimuth to Platform: 45

Observer Field of View: Angular Focusing

FOV (rad): 0.04

FOV center (m): varies; see Figure 16

Beam to be Observed: Platform to Target

A.2 LEEDR

The LEEDR settings given here are used for all phase function output presented in this project. The LEEDR Mie-calculation code is altered specifically for this project to hold the index of refraction constant, as described in Chapter 3. The only variation is with the imaginary index, which is embedded in the code and not a user input parameter as described here. Settings are input based on the conditions under which the field images are taken. Not all input sections and tabs are used. For example, default settings are used for clouds and rain, which are no clouds or rain, because laser field operation and images were conducted on clear nights. For any input section or tab not mentioned here, default settings are used.

A.2.1 Location tab

Latitude: 39.83

Longitude: -84.05

ExPERT Site: DAYTON/WRIGHT-PATTERSON

A.2.2 Atmosphere tab

Database: ExPERT

Season: Winter

Time of Day: 00-03

RH Bin Percentile: 50

Aerosols: GADS; Multiplier: 1

A.2.3 Laser/Geometry tab

Path Resolution (layers): 500

Laser Wavelength: User Wavelength

User Wavelength: 0.527e-6

Path Type: Slant Path

Platform Altitude (m): 3

Target Altitude (m): 100,000

Path Length (m): 141,500

A.2.4 Ground Level tab

Pressure (mb): 1024

Air Temperature (F): 38

Relative Humidity (%): 83

Bibliography

Andrews, Elisabeth, P.J. Sheridan, J.A. Ogren, D.H. Hageman, A. Jefferson, J. Wendell, A. Alastuey, L. Alados-Arboledas, M. Bergin, M. Ealo, A.G. Hallar, A. Hoffer, A. Hoffer, I. Kalapv, M. Keywood, J. Kim, S. Kim, F. Kolonjari, C. Labuschagne, N. Lin, A. Macdonald, O.L. Mayol-Bracero, I.B. McCubbin, M. Pandolfi, F. Reisen, S. Sharma, J.P. Sherman, M. Sorribas, and J. Sun. "Overview of the NOAA/ESRL Federated Aerosol Network," *Bull. Amer. Meteor. Soc.*, 100: 123-135 (January 2019).

Andrews, Elisabeth, P.J. Sheridan, J.A. Ogren, D.H. Hageman, A. Jefferson, J. Wendell, A. Alastuey, L. Alados-Arboledas, M. Bergin, M. Ealo, A.G. Hallar, A. Hoffer, A. Hoffer, I. Kalapv, M. Keywood, J. Kim, S. Kim, F. Kolonjari, C. Labuschagne, N. Lin, A. Macdonald, O.L. Mayol-Bracero, I.B. McCubbin, M. Pandolfi, F. Reisen, S. Sharma, J.P. Sherman, M. Sorribas, and J. Sun. "Supplemental: Overview of the NOAA/ESRL Federated Aerosol Network," *Bull. Amer. Meteor. Soc.*, 100: ES27-ES35 (January 2019).

Barnard, J., J. Fast, G. Paredes-Miranda, W. Arnott, and A. Laskin. "Technical Note: Evaluation of the WRF-Chem Aerosol Chemical to Aerosol Optical Properties Module using Data from the MILAGRO campaign," *Atmos. Chem. Phys*., 10, 7325-7340 (2010).

Bartell, R.J., G.P. Perram, S.T. Fiorino, S.N. Long, M.J. Houle, C.A. Rice, Z.P. Manning, M.J. Krizo, D.W. Bunch, and L.E. Gravley, "Methodology for comparing worldwide performance of diverse weight-constrained high energy laser systems," *Proc. SPIE* 5792: 76–87 (2005).

Belton, S.L. The Simulation of Off-Axis Laser Propagation Using HELEEOS. MS Thesis, AFIT /GSS/ENP/06-01. Graduate School of Engineering and Management, Air Force Institute of Technology (AETC), Wright-Patterson AFB OH, March 2006.

Bergstrom R.W., P. Pilewskie, P.B. Russell, J. Redemann, T.C. Bond, P.K. Quinn, et al. "Spectral absorption properties of atmospheric aerosols," *Atmos. Chem. Phys*., 7(23), 5937-43 (2007).

Bond T.C., T.L. Anderson, and D. Campbell. "Calibration and Intercomparison of Filter-Based Measurements of Visible Light Absorption by Aerosols," *Aerosol Science & Technology*, 30(6), 582-600 (2010).

Burley J.L., S.T. Fiorino, B.J. Elmore, J.E. Schmidt. "A Fast Two-Stream-Like Multiple-Scattering Method for Atmospheric Characterization and Radiative Transfer," *J. Appl. Meteol. Climatol*., 56: 3049-3063 (August 2017).

Chin, M., T. Diehl, Q. Tan, J.M. Prospero, R.A. Kahn, L.A. Remer, H. Yu, A.M. Sayer, H. Bian, I.V. Geogdzhayev, B.N. Holben, S.G. Howell, B.J. Huebert, N.C. Hsu, D. Kim, T.L. Kucsera, R.C. Levy, M.I. Mishchenko, X. Pan, P.K. Quinn, G.L. Schuster, D.G. Streets, S.A. Strode, O. Torres, and X.P. Zhao. "Multi-decadal aerosol variations from 1980 to 2009: a perspective from observations and a global model," *Atmos. Chem. Phys*., 14: 3657-3690 (2014).

Crippa P., R.C. Sullivan, A. Thota, and S.C. Pryor. "Evaluating the skill of high-resolution WRF-Chem simulations in describing drivers of aerosol direct climate forcing on the regional scale." *Atmos. Chem. Phys*., 16: 397-416 (2016).

Fiorino, S.T., J.A. Deibel, P.M. Grice, M.H. Novak, J. Spinoza, L. Owens, and S. Ganti. "A technique to measure optical properties of brownout clouds for modeling terahertz propagation." *Applied Optics*, 51: 3605-3613 (2012).

Fiorino, S.T., R.J. Bartell, G.P. Perram, D.W. Bunch, L.E. Gravley, C.A. Rice, Z.P. Manning, and M. J. Krizo, "The HELEEOS atmospheric effects package: A probabilistic method for evaluating uncertainty in low-altitude high energy laser effectiveness," *J. Dir. Energy*, 1: 347–360 (2006).

Fiorino, S.T., R.M. Randall, M.F. Via, J.L. Burley. "Validation of a U-V-to-RF High Spectral-Resolution Atmospheric Boundary Layer Characterization Tool," *J. Appl. Meteol. Climatol*., 53:136-156 (September 2014).

Fiorino, S.T., R.M. Randall, R.J. Bartell, J.D. Haiducek, M.F. Spencer, S.J. Cusumano. "Field measurements and comparisons to simulations of high energy laser propagation and off-axis scatter," *Proc. SPIE 7814, Free-Space Laser Communications X*. 78140P: 1-11 (August 2010).

Fiorino S.T., S.E. Peckham, J.E. Schmidt, and K.J. Keefer. "Evaluation of Aerosol Characterizations within the WRF-Chem GOCART Scheme," In prep for *J. Atmospheric and Oceanographic Tech (JTECH)*, 17 January 2019.

Grell, G.A., S.E. Peckham, R. Schmitz, S.A. McKeen, G. Frost, W.C. Skamarock, and B. Eder. "Fully Coupled 'online' Chemistry within the WRF Model," *Atmos. Environ*. 39 (37): 583 6957-75 (2005).

Haiducek, John. *Experimental Validation Techniques for the HELEEOS Off-Axis Laser Propagation Model*. MS Thesis, AFIT/GE/ENP/10-M02. Graduate School of Engineering and Management, Air Force Institute of Technology (AETC), Wright-Patterson AFB OH, March 2010.

Hansen, J. E., M. Sato, and R. Ruedy. “Radiative forcing and climate response” *J. Geophys. Res.*, 102: 6831–6864 (1997).

Hess, M., P. Koepke, and I. Schult. “Optical Properties of Aerosol and Clouds: The Software Package OPAC,” Bull. Amer. Meteor. Soc., 79, No. 5: 831-844 (May 1998).

Holben B.N., T.F. Eck, I. Slutsker, D. Tanre, J.P. Buis, A. Setzer, E. Vermote, J.A. Reagan, Y. Kaufman, T. Nakajima, F. Lavenu, I. Jankowiak, and A. Smirnov. “AERONET - A federated instrument network and data archive for aerosol characterization,” *Rem. Sens. Environ.*, 66: 1-16 (1998).

Koepke, Peter, M. Hess, I. Schult, and E.P. Shettle. *Global Aerosol Data Set: Report No. 243*. Hamburg Germany, Max-Planck-Institut fur Meteorologie, September 1997.

Lee, H., O.V. Kalashnikova, K. Suzuki, A. Braverman, M.J. Garay, and R.A. Kahn. “Climatology of the aerosol optical depth by components from the Multi-angle Imaging Spectroradiometer (MISR) and chemistry transport models,” *Atmos. Chem. Phys*., 16: 6627-6640 (2016).

Lin, Z. and X. Wang. “Dehazing for Image and Video Using Guided Filter,” J. of Applied Sciences, 10:123-127 (2012).

Liou, K.N. *An Introduction to Atmospheric Radiation* (2nd Edition). Academic Press, 2002.

Moosmuller, H., R.K. Chakrabarty, and W.P. Arnott. “Aerosol light absorption and its measurement: A review,” *J. Quantitative Spectroscopy & Radiative Transfer*, 110: 844–878 (2009).

Peralta, S., and P. Enrique. *Aerosol predictions and their links to weather forecasts through online interactive atmospheric modeling and data assimilation*. Ph.D. Dissertation (Doctor of Philosophy), University of Iowa, 2013.

Perram, G.P., S.J. Cusumano, R.L. Hengehold, and S.T. Fiorino. *Introduction to Laser Weapon Systems*. Albuquerque, NM: Directed Energy Professional Society, 2010.

Petty, G.W. *A First Course in Atmospheric Radiation* (2nd Edition). Madison, WI: Sundog Publishing, 2006.

Remer, L.A., R.G. Kleidman, R.C. Levy, Y.J. Kaufman, D. Tanré, S. Mattoo, J.V. Martins, C. Ichoku, I. Koran, H. Yu, and B.N. Holben. “Global aerosol climatology from the MODIS satellite sensors,” *J. Geophys. Res.-Atmos*., 113: D14S07, (2008).

Samset B.H., C.W. Stern, E. Andrews, R.A. Kahn, G. Mire, M. Schulz, and G.L. Schuster. “Aerosol Absorption: Progress towards Global and Regional Constraints,” *Current Climate Change Reports*, 4:65-83 (June 2018).

Stephens, G.L. *Remote Sensing of the Lower Atmosphere*. New York: Oxford University Press, 1994

REPORT DOCUMENTATION PAGE

Form Approved
OMB No. 0704-0188

1. REPORT DATE *(DD-MM-YYYY)*	**2. REPORT TYPE**	**3. DATES COVERED** *(From - To)*
03/26/2020	Master's Thesis	Aug 2018 - Mar 2020

4. TITLE AND SUBTITLE
Determining Bulk Aerosol Absorption from Off-Axis Backscattering using Rayleigh Beacon Laser Pulses

5a. CONTRACT NUMBER

5b. GRANT NUMBER

5c. PROGRAM ELEMENT NUMBER

6. AUTHOR(S)
Grossnickle, Julie C, Maj, USAF

5d. PROJECT NUMBER

5e. TASK NUMBER

5f. WORK UNIT NUMBER

7. PERFORMING ORGANIZATION NAME(S) AND ADDRESS(ES)
Air Force Institute of Technology
Graduate School of Engineering and Management (AFIT/EN)
2950 Hobson Way
Wright-Patterson AFB OH 45433-7765

8. PERFORMING ORGANIZATION REPORT NUMBER
AFIT-ENP-MS-20-M-097

9. SPONSORING/MONITORING AGENCY NAME(S) AND ADDRESS(ES)
Directed Energy - Joint Transition Office
801 University Blvd. SE, Suite 100
Albuquerque, NM 87106

10. SPONSOR/MONITOR'S ACRONYM(S)
DE-JTO

11. SPONSOR/MONITOR'S REPORT NUMBER(S)

12. DISTRIBUTION/AVAILABILITY STATEMENT
Distribution Statement A. Approved for Public Release; Distribution Unlimited

13. SUPPLEMENTARY NOTES
This material is declared a work of the U.S. Government and is not subject to copyright protection in the United States.

14. ABSTRACT
Aerosol absorption plays a key role in degrading laser performance in the form of beam attenuation. Laser Environmental Effects Definition and Reference (LEEDR) and High Energy Laser End-to-End Operational Simulation (HELEEOS) modeling packages were created to model total scattered irradiance at given off-axis locations through the use of an off-axis scattering algorithm. Laser energy scattered from a Rayleigh beacon illuminator at 527 nm is measured using a visible camera. The differences in the measured versus predicted phase functions can help draw conclusions on bulk aerosol absorption properties, and lead to better quantification of degradation of laser performance due to aerosols.

15. SUBJECT TERMS
off-axis backscattering, phase functions, aerosol absorption, complex refractive index, LEEDR, HELEEOS

16. SECURITY CLASSIFICATION OF:			**17. LIMITATION OF ABSTRACT**	**18. NUMBER OF PAGES**	**19a. NAME OF RESPONSIBLE PERSON**
a. REPORT	**b. ABSTRACT**	**c. THIS PAGE**			Dr. Steven T. Fiorino, AFIT/ENP
					19b. TELEPHONE NUMBER *(Include area code)*
U	U	U	UU	77	(937)255-3636, x4506; steven.fiorino@afit.edu